Changes in Freshwater Distribution and Pathways in the Arctic Ocean Since 2007 in the Mercator Ocean Global Operational System

Cécilia Bertosio, Christine Provost, Marylou Athanase, Nathalie Sennéchael, Gilles Garric, Jean-michel Lellouche, Clément Bricaud, Joo-hong Kim, Kyoung-ho Cho, Taewook Park

To cite this version:

Cécilia Bertosio, Christine Provost, Marylou Athanase, Nathalie Sennéchael, Gilles Garric, et al.. Changes in Freshwater Distribution and Pathways in the Arctic Ocean Since 2007 in the Mercator Ocean Global Operational System. Journal of Geophysical Research. Oceans, 2022, 127 (6), pp.e2021JC017701. 10.1029/2021JC017701 . hal-03690597

HAL Id: hal-03690597
https://hal.science/hal-03690597

Submitted on 21 Mar 2023

AGU ADVANCING EARTH AND SPACE SCIENCE

JGR Oceans

RESEARCH ARTICLE

10.1029/2021JC017701

Special Section:
Uncovering the hidden links between dynamics, chemical, biogeochemical and biological processes under the changing Arctic

Changes in Freshwater Distribution and Pathways in the Arctic Ocean Since 2007 in the Mercator Ocean Global Operational System

Cécilia Bertosio[1], Christine Provost[1], Marylou Athanase[2], Nathalie Sennéchael[1], Gilles Garric[3], Jean-Michel Lellouche[3], Clément Bricaud[3], Joo-Hong Kim[4], Kyoung-Ho Cho[4], and Taewook Park[4]

[1]Laboratoire LOCEAN-IPSL, Sorbonne Université (UPMC, University Paris 6), CNRS, IRD, MNHN, Paris, France, [2]Alfred-Wegener-Institute, Bremerhaven, Germany, [3]MERCATOR-OCEAN, Toulouse, France, [4]Division of Polar Ocean Sciences, Korea Polar Research Institute, Incheon, Republic of Korea

Key Points:

- The Mercator Ocean model was capable of reproducing observed spatial patterns of Arctic freshwater content and sea surface height
- After 2012, waters in the Makarov Basin near the North Pole freshened and Atlantic-origin waters shoaled along the East Siberian slope
- After 2015, liquid freshwater outflow increased through the western Canadian Archipelago and decreased through Fram Strait

Supporting Information:

Supporting Information may be found in the online version of this article.

Correspondence to:

C. Bertosio, C. Provost, and M. Athanase,
cecilia.bertosio.espci@gmail.com;
cp@locean-ipsl.upmc.fr;
marylou.athanase@awi.de

Citation:

Bertosio, C., Provost, C., Athanase, M., Sennéchael, N., Garric, G., Lellouche, J.-M., et al. (2022). Changes in freshwater distribution and pathways in the Arctic Ocean since 2007 in the Mercator Ocean global operational system. *Journal of Geophysical Research: Oceans*, *127*, e2021JC017701. https://doi.org/10.1029/2021JC017701

Received 24 JUN 2021
Accepted 19 MAY 2022

Abstract Low-salinity waters in the upper Arctic Ocean, referred to as “freshwaters”, are cold and play a major role in isolating the sea ice cover from the heat stored in the salty Atlantic Waters (AW) underneath. We examined changes in Arctic freshwater distribution and circulation since 2007 using the 1/12° global Mercator Ocean operational model. We first evaluated model simulations over the upper water column in the Arctic Ocean, using nearly 20,000 independent in situ temperature-salinity profiles over the 2007–2020 period. Simulated hydrographic properties and water mass distributions were in good agreement with observations. Comparison with long-term mooring data in the Bering Strait and Beaufort Gyre highlighted the model's capabilities for reproducing the interannual evolution of Pacific Water properties. Taking advantage of the good performance of the model, we examined the interannual evolution of the freshwater distribution and circulation over 2007–2020. The Beaufort Gyre is the major freshwater reservoir across the full Arctic Ocean. After 2012 the gyre extended northward and increased the freshwater content in the Makarov Basin, near the North Pole. Coincidentally, the freshwater content decreased along the East Siberian slope, along with the AW shoaling, and the Transpolar Drift moved from the Lomonosov Ridge to align with the Mendeleev Ridge. We found that these changes in freshwater distribution were followed in 2015 by a marked change in the export of freshwater from the Arctic Ocean with a reduction in Fram Strait (−30%) and an increase in the western Canadian Archipelago (+16%).

Plain Language Summary We evaluated 14 years of simulations from a high-resolution ocean model to identify changes in the upper water column of the Arctic Ocean since 2007. Comparisons of simulations with observations highlighted the model's capabilities for reproducing the properties of the Arctic Ocean. We then examined how the freshwaters, which isolate the sea-ice from the heat stored at depth, have seen their distribution and pathways changed over the last 14 years in the model. The freshwater content increased near the North Pole after 2012, while one of the largest reservoirs of freshwater in the Arctic Ocean retreated to the northeast. We also documented changes in the freshwater pathway exiting the Arctic with more freshwater outflow through the western Canadian Archipelago after 2015.

1. Introduction

In contrast with the midlatitudes and tropics, the stratification of the Arctic Ocean is essentially salinity-driven (Carmack, 2007; Timmermans & Jayne, 2016). Low-salinity waters of the upper water column are cold and play a major role in isolating sea ice at the surface from the heat carried by the underlying Atlantic Waters (AW, defined as $S_A > 34.9$ g kg^{-1}, $\Theta > 0$°C; Rudels et al., 1996). The low-salinity waters (with a wide range of salinities $0 < S_A < 34.9$ g kg^{-1}), which make up the halocline and the surface mixed layer, are commonly called freshwaters (e.g., Karpouzoglou et al., 2022; Proshutinsky et al., 2019; Rabe et al., 2014; Z. Wang et al., 2017). Freshwater inputs to the Arctic Ocean comprise three sources: continental runoff, Pacific-derived water, and net precipitation (e.g., Aagaard & Woodgate, 2001; McClelland et al., 2012; Serreze et al., 2006). During the 2000–2010 period, the continental runoff was estimated at ~133 mSv, the Pacific-derived freshwater input at ~82 mSv, and precipitation at ~70 mSv (Haine et al., 2015; Rabe et al., 2014; 1 mSv = 1 milliSverdrup = 10^3 m^3 s^{-1}).

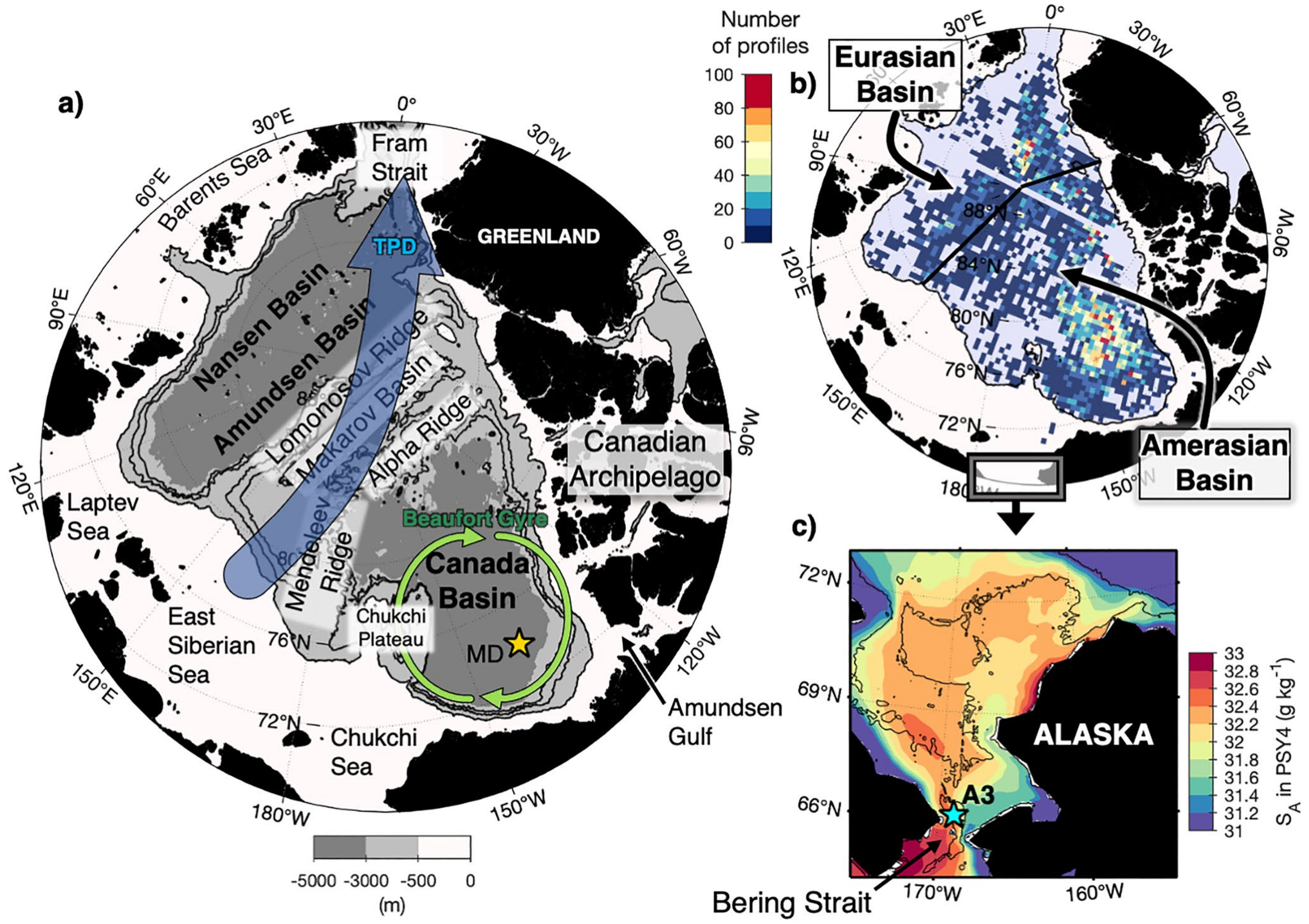

Figure 1. (a) Main geographic/bathymetric features. Transpolar Drift (TPD) and Beaufort Gyre are indicated with blue and green arrows respectively. Bathymetry contours correspond to 2,500, 2,000, and 50 m from IBCAO. (b) Number of profiles used in this study over the 2007–2014 period. Isobath 500 m is shown in black. The thin black line, corresponding to the Lomonosov Ridge, separates the Eurasian from the Amerasian Basin. (c) Close-up of the Bering Strait and the Chukchi Sea. Background colors correspond to PSY4 Absolute Salinity values over 2007–2020 (at 5 m depth). The yellow star in (a) marks the location of BGEP mooring D (MD). The blue star in (c) indicates the location of mooring A3. Bathymetry contours are for depths 50 and 500 m.

The distribution of freshwater content (FWC) in the Arctic Ocean is governed by wind-driven and density-driven oceanic circulation. The combined effects result in a non-uniform distribution over the Arctic domain with a maximum FWC in the Canada Basin and a minimum in the Nansen Basin (Figure 1a). The wind-driven ocean circulation features the Transpolar Drift (TPD), a stream transporting sea ice and relatively fresh waters from the Siberian shelves across the Arctic toward the Fram Strait (e.g., Morison et al., 2012, 1998), and the Beaufort Gyre (BG), a large-scale gyre dominating the Canada Basin circulation (Figure 1a). Studies showed that upper ocean circulation regime changes are linked to the variations of the Arctic Oscillation index (e.g., Armitage et al., 2018; Karcher et al., 2012; Morison et al., 2012; Q. Wang, 2021). The Arctic Oscillation index is derived from patterns of sea level pressure anomalies and reflects a back-and-forth shift of atmospheric pressure between the Arctic and the mid-latitudes of the North Pacific and North Atlantic (Thompson & Wallace, 1998). Positive values of the Arctic Oscillation index denote a strengthened cyclonic (anticlockwise) ocean circulation regime in the Eurasian Basin, a TPD toward Mendeleev Ridge and a strong anticyclonic (clockwise) BG restricted to the Canada Basin (Figure 1; e.g., Morison et al., 2021, 2012, 1998; Swift et al., 1997; Q. Wang, 2021). Negative Arctic Oscillation index values correspond to a TPD toward the Lomonosov Ridge (Morison et al., 2021) and an extended anticyclonic BG in the Amerasian Basin. Q. Wang (2021) additionally showed that during negative Arctic Oscillation index periods, FWC increases in the central Arctic.

The BG is governed by wind stress, dynamic feedback between ice motion and upper ocean current, and lateral eddy fluxes (Doddridge et al., 2019). The resulting surface stress leads to an Ekman convergence and freshwater accumulation toward the center of the gyre (Proshutinsky et al., 2002, 2015, 2009). The FWC variability is associated with sea surface height (SSH) variations through the halosteric effect (i.e., saline contraction or expansion of a water parcel), thus variations in SSH patterns are good indicators of changes in the FWC distribution (Armitage et al., 2016; Q. Wang, 2021). Recent satellite observations of SSH indicated a northwestward expansion of the Beaufort Gyre from 2003 to 2014, resulting from an intensification and pattern change in the wind stress field (Regan et al., 2019). The center of the BG is characterized by a maximum SSH and a thick and strong halocline (Polyakov et al., 2018; Regan et al., 2019). The BG halocline comprises Pacific Waters that enter the Arctic via the Bering Strait (Figure 1; Proshutinsky et al., 2019; Shimada et al., 2005). Seasonal processes modify Pacific Waters before they reach the BG halocline. In summer, solar input and ice melt warm and freshen the Pacific Summer Waters (PSW; $31 < S_A < 32$ g kg^{-1}; $-1 < \Theta < 1$°C). In winter, ice formation and brine release cool and increase the salinity of Pacific Winter Waters (PWW; $32.2 < S_A < 33.2$ g kg^{-1}; $\Theta \sim -1.8$°C; Timmermans & Marshall, 2020; Woodgate & Peralta-Ferriz, 2021).

The BG constitutes the largest freshwater reservoir of the Arctic Ocean, it stores approximately $23{,}000 \pm 2{,}000$ km^3 of freshwater and accumulated an additional 6,400 km^3 of freshwater over the last decade (Carmack et al., 2016; Proshutinsky et al., 2019). Proshutinsky et al. (2019) showed that the freshwater increase in the gyre largely resulted from a redirection of nearby river discharge and Pacific Water contribution. This increase in freshwater storage in the BG was concomitant with a steady increase in pan-Arctic FWC from the early 1990s until 2007 (Proshutinsky et al., 2019; Rabe et al., 2014; Solomon et al., 2020; Q. Wang, 2021). After 2007, the Arctic freshwater reached a plateau due to compensation between an FWC increase in the BG and an FWC decrease in the other basins (Solomon et al., 2020).

Under dominant cyclonic winds, the freshwater accumulated in the gyre can be released into the larger Arctic Ocean (Proshutinsky et al., 2002; Proshutinsky & Johnson, 1997; Zhang et al., 2021; Zhong et al., 2019) and eventually discharged to the North Atlantic through Fram Strait (~ 89 mSv over 2000–2010; Haine et al., 2015) and the Canadian Archipelago (~68 mSv before 2006; Beszczynska-Möller et al., 2011). The Arctic freshwater outflow is a key feature impacting the large-scale circulation in the North Atlantic Ocean, such as the Atlantic Meridional Overturning Circulation which is driven by vertical density gradients. Hence, an excessive freshwater release could reduce surface ocean density and weaken the Atlantic Meridional Overturning Circulation (Rahmstorf et al., 2015; Zhang et al., 2021). Monitoring the recent evolution of the FWC distribution in the Arctic is thus crucial to increasing our understanding of the ongoing Arctic changes and their potential impact at lower latitudes.

Despite significant international efforts in the last decade (e.g., Koenig, Provost, Villacieros-Robineau, et al., 2017; Toole et al., 2011), hydrographic data remain sparse in the Arctic (Behrendt et al., 2018). Coupled ocean-sea ice operational analysis systems helped interpret observations in this region (e.g., Zhang et al., 2016). The Mercator Ocean operational 1/12° physical system PSY4 (Lellouche et al., 2018) has proven capable of reproducing the hydrography, mesoscale structures, and seasonal signals in the western Nansen Basin (Athanase et al., 2019; Koenig, Provost, Sennéchael, et al., 2017). PSY4 provided insights on the development of new pathways of AW, the intensification of the circulation north of Svalbard, the progressive warming and thickening of the AW layer (Athanase et al., 2021) and documented interannual variations of winter mixed layers and processes modifying AW (Athanase et al., 2020).

This paper aims to further assess PSY4 capabilities over the Arctic deep basins and to use the 14 years simulation to investigate changes in freshwater distribution and pathways in the Arctic Ocean since 2007. In particular, we examine whether the northwestward extension of the BG beyond the Chukchi Plateau (Figure 1) documented until 2014 (Regan et al., 2019) is a temporary shift or a new geographical position for the gyre.

Section 2 introduces the Mercator Ocean operational system and describes the independent in situ data used to evaluate the model. The performance of the model is assessed over the Arctic Ocean halocline in Section 3. In Section 4, we investigate the interannual evolution of the upper water column from 2007 onwards. Results are discussed in Section 5 and a conclusion is provided in Section 6.

2. Operational System and Non-Assimilated Data

2.1. Mercator Ocean Operational System

The global operational system PSY4 was developed at Mercator Ocean for the Copernicus Marine Environment Monitoring Service (http://marine.copernicus.eu/) and simulates physical ocean variables (e.g., temperature, salinity, SSH, and velocity) and sea ice variables from 2007 onwards (Lellouche et al., 2018). The physical configuration is based on a 1/12° tripolar grid (Madec & Imbard, 1996; grid spacing of 3–5 km in the Arctic), with 50 vertical levels of decreasing resolution from 1 m at the surface to 450 m at the bottom, including 22 levels within the upper 100 m. The system PSY4 uses version 3.1 of the Nucleus for European Modeling of the Ocean model (NEMO; Madec et al., 2008) and the Louvain-La-Neuve thermodynamic-dynamic sea Ice Model (LIM2, Fichefet & Maqueda, 1997). At the surface, the model is driven by atmospheric analyses and forecasts obtained from the European Center for Medium-Range Weather Forecasts-Integrated Forecast System (ECMWF-IFS) at 3 hr resolution. Apart from sea ice concentrations (from Ocean Sea Ice-Satellite Application Facilities products, https://doi.org/10.48670/moi-00134), no assimilation is performed in the ice-covered ocean in the Arctic. The PSY4 system was initialized in October 2006 using quality-controlled ocean temperature and salinity profiles from the data set EN4.2.1 (Good et al., 2013). Details about initialization and bathymetry used in PSY4 are given in Supporting Information. So far, PSY4 evaluations in the Arctic have focused on the upper 600 m of the western Eurasian Basin. The model performed adequately in simulating sea ice cover, temperature, salinity, and ocean currents, as well as reproducing observed mesoscale structures (e.g., Athanase et al., 2020, 2019; Koenig, Provost, Sennéchael, et al., 2017; Koenig, Provost, Villacieros-Robineau, et al., 2017).

2.2. Particle Tracking Method

We used daily horizontal model velocities to investigate the possible origin and fate of water parcels. Lagrangian backward and forward trajectories of synthetic particles were tracked using a simple prediction correction scheme similar to that employed by Fillipi et al. (2010) and previously used in Bertosio et al. (2020). We released 160 particles in a box spanning the BG region 72°–79°N, 170°W–130°W, and 160 particles in another box in the central Makarov Basin spanning the region 86.5°–88°N, 150°W–175°W. Particles were released at depths of 5, 80, and 150 m. In this study, we only show results at 80 m depth. We performed two launches every year from 2007 to 2020: one at the end of the winter and one at the end of the summer. We tracked the particles for 6 years. For clarity, we only showed the first 3 years. We displayed the trajectories on maps using a grid of 25 × 10 km and counting when each trajectory crosses the grid cell. Trajectories of water parcels and time scales of advection are examined in Section 4.

2.3. Non Assimilated Data for Model Evaluation

A total of 19,642 temperature and salinity profiles were gathered from several data sets: the UDASH database spanning 1980–2015 (Behrendt et al., 2018; see Figure S1 in Supporting Information S1); recent ice tethered platforms not included in UDASH (ITPs: Krishfield et al., 2008; IAOOS: Boles et al., 2020); and moorings (summary in Table 1 and data distribution in Figure 1). Quality checks were performed to remove erroneous profiles. Mooring D (Figure 1a) from the Beaufort Gyre Exploration Project (BGEP) deployed in the Canada Basin provided continuous time series of temperature, salinity, and ice draft data over the 2007–2018 period (http://www.whoi.edu/beaufortgyre, see Proshutinsky et al., 2009 for further details). In the Bering Strait, the A3 mooring (Figure 1c) recorded near-bottom (48 m) temperature and salinity data, and velocity profiles over the 2007–2019 period (Woodgate, 2018; Woodgate et al., 2015, 2012). Daily PSY4 fields were collocated in time and space (closest grid cell) with the in situ profiles. We linearly interpolated profiles from both in situ measurements and PSY4 simulated data (with a variable vertical resolution, cf. Section 2.1) to the same 2 m vertical resolution to ease model-observations comparisons.

SSH fields from PSY4 were compared to the altimetry products from Armitage et al. (2017, 2016; called CPOM hereafter) spanning the 2007–2014 period. PSY4 SSH fields were interpolated to the coarser CPOM grid (0.75° × 0.25° longitude/latitude grid).

PSY4 sea ice concentration and thickness were compared to those from the Pan-arctic Ice-Ocean Modeling and Assimilation System (PIOMAS—version 2.1). PIOMAS assimilates daily sea ice concentration

Table 1
Data Used for Model Evaluation

Data set	Parameters	Dates	Reference	Web site
UDASH database CTD	T, S 19,642 profiles	2007–2015	Behrendt et al. (2018)	*PANGEA*: https://doi.pangaea.de/10.1594/PANGAEA.872931
Drifting platforms ITPs and IAOOS		2014–2019	Athanase et al. (2019) and Krishfield et al. (2008)	*WHOI*: https://www2.whoi.edu/site/beaufortgyre/data/ *SEANOE*: https://doi.org/10.17882/57288
BERING Strait *A3* moorings	T, S, U, V	Mid-2007 to mid-2019	Woodgate (2018) and Woodgate and Peralta-Ferriz (2021)	http://psc.apl.washington.edu/HLD/Bstrait/Data/BeringStraitMooringDataArchive.html
BGEP D-moorings	T, S 2,200 profiles	2007–2018	Proshutinsky et al. (2009)	*WHOI*: https://www2.whoi.edu/site/beaufortgyre/data/
CPOM	SSH	2007–2014	Armitage et al. (2016, 2017)	http://www.cpom.ucl.ac.uk/dynamic_topography/
PIOMAS	Ice thickness	2007–2019	Schweiger et al. (2011) and Zhang et al. (2003)	http://psc.apl.uw.edu/research/projects/arctic-sea-ice-volume-anomaly/data/model_grid

(from NSIDC) and sea surface temperature (from the NCEP/NCAR reanalysis) and has been extensively validated (e.g., Schweiger et al., 2011; X. Wang, Key, et al., 2016). The PIOMAS grid is ∼22 km resolution, which is coarser than the PSY4 grid (3–5 km in the Arctic). PSY4 fields were spatially downsampled to the PIOMAS grid to enable the comparison. A comparison of PSY4 with the PIOMAS sea ice data is listed in the Supporting Information.

2.4. Freshwater Content and Available Potential Energy (APE) Computations

Absolute Salinity S_A (g kg^{-1}) and Conservative Temperature Θ (°C) are used following the TEOS-10 (Thermodynamic Equations of Seawater) international standard (McDougall & Barker, 2011). However, FWC calculations were performed with practical salinity (not Absolute Salinity) to facilitate comparison with literature values. The FWC was computed relative to salinity 34.8 psu (∼34.97 g kg^{-1} in Absolute Salinity) following Proshutinsky et al. (2009):

$$\mathrm{FWC} = \int_{z_{34.8}}^{z_1} \frac{34.8 - S(z)}{34.8}\, dz \tag{1}$$

where z_1 = surface. The total freshwater volume over the Arctic basins in the model was obtained by summing the FWC multiplied by the model grid cell area when the seafloor was deeper than 500 m. We additionally computed freshwater volume outflow at several gateways of the Arctic such as:

$$\text{Freshwater volume outflow} = \int_{z_{34.8}}^{z_1} \frac{34.8 - S(z)}{34.8} \times v(z) \times A(z)\, dz \tag{2}$$

where v is the velocity and A is the surface associated with the model grid cell at depth z.

The sea ice cover is better isolated from the underneath warm AW when the upper water column is strongly stratified (i.e., vertical density gradients are large). To quantify the strength of the stratification in the complex upper water column of the Arctic Ocean, halocline water masses, and surface mixed layer, we used the bulk metric of the APE, initially proposed by Polyakov et al. (2018). At each location, it is calculated as:

$$\mathrm{APE} = \int_{z_{27.85}}^{\text{surface}} g(\sigma(z) - 27.85) z\, dz \tag{3}$$

where g is the gravitational constant and σ is the density anomaly (in kg m^{-3}), referred to as density hereafter. The depth of the isopycnal 27.85 kg m^{-3} ($z_{27.85}$) was considered as the base of the halocline layer (Bertosio et al., 2020). The APE can exchange reversibly with the kinetic energy, and gives an informative integral indicator of the stratification of the Arctic Ocean. The higher the APE, the stronger the stratification in the upper water column.

3. Comparison of the Model With Observations

3.1. Model Temperature and Salinity in the Upper Layer Over Arctic Deep Basins

Athanase et al. (2020) carried out an extensive evaluation of PSY4 performance in the western Nansen Basin and Fram Strait. Here, we extended the evaluation to the Arctic deep basins. We investigated the horizontal distribution of the model-observation temperature and salinity differences by computing the root mean square error (RMSE) over the upper 400 m water column (Figures 2a and 2b). There was a contrasted distribution of the RMSE, with the largest temperature biases found in the Eurasian Basin (RMSE > 1°C) and large salinity biases located in the Makarov and Canada Basins (RMSE > 0.8 g kg^{-1}). Nevertheless, PSY4 reproduced well the observed salinity and temperature horizontal patterns. For illustration, model and observation fields at the near-surface (0–20 m), in the halocline (80–100 m), and in the AW layer (180–200 m) are shown in Figure S2 in Supporting Information S1. Additionally, we investigated the vertical distribution of the differences along a transect crossing the Arctic basins by using the spatially closest profiles (Figures 2c–2h). Note that sections along this transect are composites, comprising profiles from different years and different months. In the following analyses, we first consider the Eurasian Basin and then focus on the Canada and Makarov Basins separately.

3.1.1. The Eurasian Basin

In the Eurasian Basin, temperature differences were large along the continental slope, especially in the eastern Nansen Basin (Figure 2a). Vertical profiles featured a cold bias at 80–150 m where AW lies ($-1 < \Delta\Theta < -0.5$°C, Table 2), particularly pronounced in the core of the boundary current (Figures 2c–2e). A portion of the cold bias is likely explained by an erroneously cold upstream AW core in Fram Strait (where $\Delta\Theta \sim -0.2$°C, c.f. Athanase et al., 2020). However, negative temperature biases in the eastern Nansen Basin exceeded those in the Fram Strait, possibly resulting from overestimated convective processes in the Eurasian Arctic which amplified the cold bias in the AW layer.

In contrast, salinity biases in the Eurasian Basin were small (RMSE < 0.4 g kg^{-1}, Figure 2b). Below 80 m in the AW core, modeled salinities were close to the observations ($|\Delta S_A| < 0.04$ g kg^{-1}, Table 2, Figures 2f–2h). The largest salinity biases were restricted to the upper 60 m, where modeled polar surface waters were saltier than in observations ($0 < \Delta S_A < 0.5$ g kg^{-1}, Table 2). Many climate models have similar surface salinity biases as processes near the surface are complex and the variability is large (Lique et al., 2016). However, data points available over the 2007–2020 period in the Eurasian Basin were insufficient to further investigate the surface salinity bias; most of the observations were from the summer period and the spacing was poor (Figure S1 in Supporting Information S1).

3.1.2. The Makarov and Canada Basins

In the Makarov Basin, temperature biases were small compared to that in the Eurasian Basin (RMSE < 0.4°C, Figure 2a). The modeled halocline was slightly too warm ($\Delta\Theta \sim +0.25$°C), while the modeled AW (found below the 27.8 isopycnal) remained deeper and colder than in the observations ($\Delta z \sim 50$m, $\Delta\Theta \sim -0.2$°C; Figures 2c–2e). The modeled salinity in the upper 50 m was larger than observations by ~1–2 g kg^{-1} (Figure 2h, Table 2). Several sources can contribute to this surface salinity bias, such as too little (or too much) simulated brine rejection from sea ice growth or biases in the redistribution of modeled river discharge. In the Makarov Basin, modeled sea ice thickness and concentration were similar to the extensively evaluated reanalysis PIOMAS (see Supporting Information). Therefore, sea ice is unlikely the primary contributor to the bias. The Makarov Basin surface waters are influenced by shelf waters from the Siberian Sea (Figure 1). One possibility would be that the surface salinity bias originated from the shelf area and was advected toward the basin. Modeled river discharge inputs and model performances over the shelves still need to be further investigated to determine the cause of the surface salinity bias in PSY4.

The Canada Basin benefits from a more extensive spatial and temporal measurement coverage compared to the Eurasian Basin, as numerous drifting platforms were deployed in the BG area providing year-round data (Figure S1 in Supporting Information S1). The Canada Basin upper water column comprises the surface mixed layer (in the upper 50 m), the PSW (50–100 m), PWW (100–200 m), and AW (below 300–350 m; Figure 3a). The PSW, characterized by a local temperature maximum in the upper 100 m, were on average colder, saltier, and therefore denser and deeper in the model compared to observations ($\Delta\Theta \sim -1$°C ± 0.4°C, $\Delta S_A \sim 0.3$ g kg^{-1}, $\Delta\sigma \sim 0.3$ kg m^{-3}, $\Delta z \sim 30$ m; Figures 2c–2e, Figures 3a–3f). In contrast, the underlying PWW, characterized by a temperature

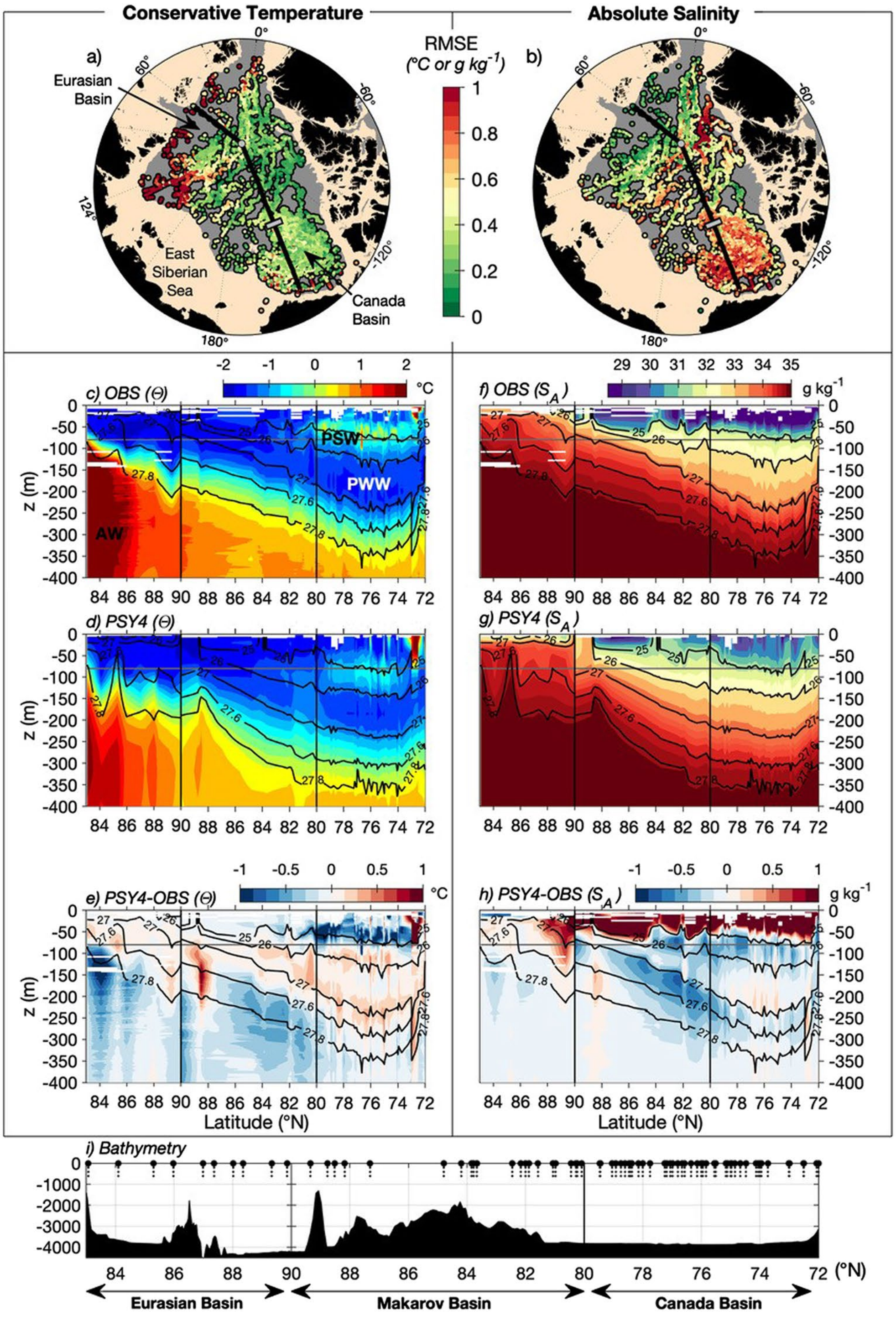

Figure 2. Comparison of the Conservative Temperature Θ (°C) and Absolute Salinity S_A (g kg^{-1}) between PSY4 and in situ data from UDASH and ITPs. (a) Horizontal distribution of the root-mean-square error (RMSE) of Θ over the upper 400 m. (b) same as (a) for S_A. Background in gray corresponds to bathymetry deeper than 400 m. The line indicates the location of the section shown below, with a gray tick at 80°N and a gray dot at 90°N for sake of readability. (c) Vertical sections of temperature obtained from in situ profiles closest to the section. Isopycnals are shown in black. The *x*-axis is latitude (°N). Horizontal gray lines correspond to the depth 80 m. (d) same as (c) with collocated PSY4 profiles. (e) Temperature differences PSY4-OBS. (f–h) Same as (c–e) for S_A. (h) Bathymetry below the section that crosses the Eurasian Basin, Makarov Basin, and Canada Basin. Positions of profiles used for the composite sections are indicated. *PWW, Pacific Winter Waters; PSW, Pacific Summer Waters; AW, Atlantic Water*.

Table 2
*Statistics of Θ and S_A Model-Observation Differences at Several Layers in the Eurasian and Amerasian Basin**

		Eurasian basin				Amerasian basin			
	Layer (m)	Mean	CI (95%)	STD	RMSE	Mean	CI (95%)	STD	RMSE
$\Delta\Theta$ (°C)	0–20	−0.03	[−0.03; −0.02]	0.2	0.2	−0.11	[−0.12; −0.11]	0.2	0.2
	40–60	+0.05	[+0.05; +0.06]	0.2	0.6	−0.38	[−0.39; −0.37]	0.5	0.6
	80–100	+0.15	[+0.14; +0.16]	0.4	0.3	−0.039	[−0.043; −0.035]	0.2	0.3
	140–160	−0.12	[−0.13; −0.10]	0.6	0.3	+0.11	[+0.11; +0.12]	0.2	0.3
	180–200	−0.30	[−0.30; −0.27]	0.6	0.4	+0.086	[+0.082; +0.09]	0.2	0.4
	240–260	−0.34	[−0.35; −0.32]	0.4	0.3	−0.07	[−0.07; −0.07]	0.3	0.3
	320–340	−0.26	[−0.27; −0.25]	0.3	0.3	−0.14	[−0.14; −0.14]	0.2	0.3
	400–420	−0.22	[−0.23; −0.21]	0.3	0.2	−0.11	[−0.11; −0.11]	0.1	0.2
ΔS_A (g.kg^{-1})	0–20	+0.51	[+0.46; +0.53]	1.2	2.2	+2.0	[+1.98; +2.01]	1.2	2.2
	40–60	+0.36	[+0.34; +0.39]	0.8	0.9	+0.57	[+0.56; +0.58]	0.7	0.9
	80–100	0.00	[−0.01; +0.01]	0.3	0.4	−0.19	[−0.19; −0.18]	0.4	0.4
	140–160	−0.03	[−0.04; −0.03]	0.1	0.2	−0.08	[−0.09; −0.08]	0.2	0.2
	180–200	−0.04	[−0.04; −0.04]	0.1	0.2	−0.10	[−0.10; −0.09]	0.2	0.2
	240–260	−0.04	[−0.04; −0.04]	0.0	0.2	−0.14	[−0.15; −0.14]	0.2	0.2
	320–340	−0.01	[−0.01; −0.01]	0.0	0.1	−0.04	[−0.04; −0.04]	0.1	0.1
	400–420	−0.01	[−0.01; −0.01]	0.0	0.0	−0.02	[−0.02; −0.02]	0.0	0.0

Note. *CI, confidence interval; STD, standard deviation; RMSE, root mean square error; The confidence intervals are evaluated from a *t* test of the hypothesis that model and observation values come from distributions with equal means (and $\alpha = 0.05$).

minimum at ~ 180 m, were at the right depth, temperature, and salinity ($|\Delta\Theta| < 0.1$°C and $|\Delta S_A| < 0.1$ g kg^{-1} in the 180–200 m layer, Figures 2c–2e, Figures 3a–3f and Table 2). The modeled temperature and salinity of the Canada Basin AW layer exhibited small differences when compared to observations ($|\Delta\Theta| < 0.1$°C and $|\Delta S_A| < 0.1$ g kg^{-1} below isopycnal 27.8 kg m^{-3} in Figures 2c–2h). Salinity biases in the Canada Basin were predominantly due to an overestimation of modeled salinities in the upper 50 m by 2 g kg^{-1} (Figures 2b and 2f–2h). Such surface bias is a common feature of the state-of-the-art ocean and sea-ice models (e.g., Lique et al., 2016; Regan et al., 2020; Q. Wang, Ilicak, et al., 2016). The PSY4 sea ice thickness in the area was overestimated compared to PIOMAS, which likely contributed to an overestimation of the modeled surface salinity (see Supporting Information). The nearby river inputs in PSY4 are also an interesting possible source of the surface salinity to investigate and should be considered in future work.

To provide an overview of the evolution of biases over time, we used year-round temperature and salinity mooring data over the 2007–2018 period in the BG area (namely BGEP mooring D; Proshutinsky et al., 2019). The model performance in representing water masses described in the previous paragraphs—which are (a) colder and deeper modeled PSW and (b) a close accordance of the modeled PWW and AW properties with observations—remained unchanged over the 2007–2018 period (Figure 3). This suggested little model drift over time and it is plausible that temperature and salinity discrepancies mainly resulted from biases in the initial conditions (Figure S3 in Supporting Information S1).

The depression of modeled isopycnals induced by the BG dynamic in the Amerasian Basin matched the observations well, with isopycnal 27.8 kg m^{-3} reaching 350 m depth in the Canada Basin (vs. 200 m depth at the North Pole, Figures 2c–2g). In 2008 and 2017, PSY4 reproduced an observed downwelling of isopycnals, however, modeled isopycnal downwelling in 2016 and 2018 was too smooth (Figures 3g–3j). Consequently, the temperature and salinity at 255 m were overestimated during these 2 years, as the modeled base of the PWW layer was not deep enough (Figure 3l). Vertical salinity gradients at the base of PSW and PWW, that is, in the halocline, are large and a precise simulation of the ocean at the right depth and time is demanding.

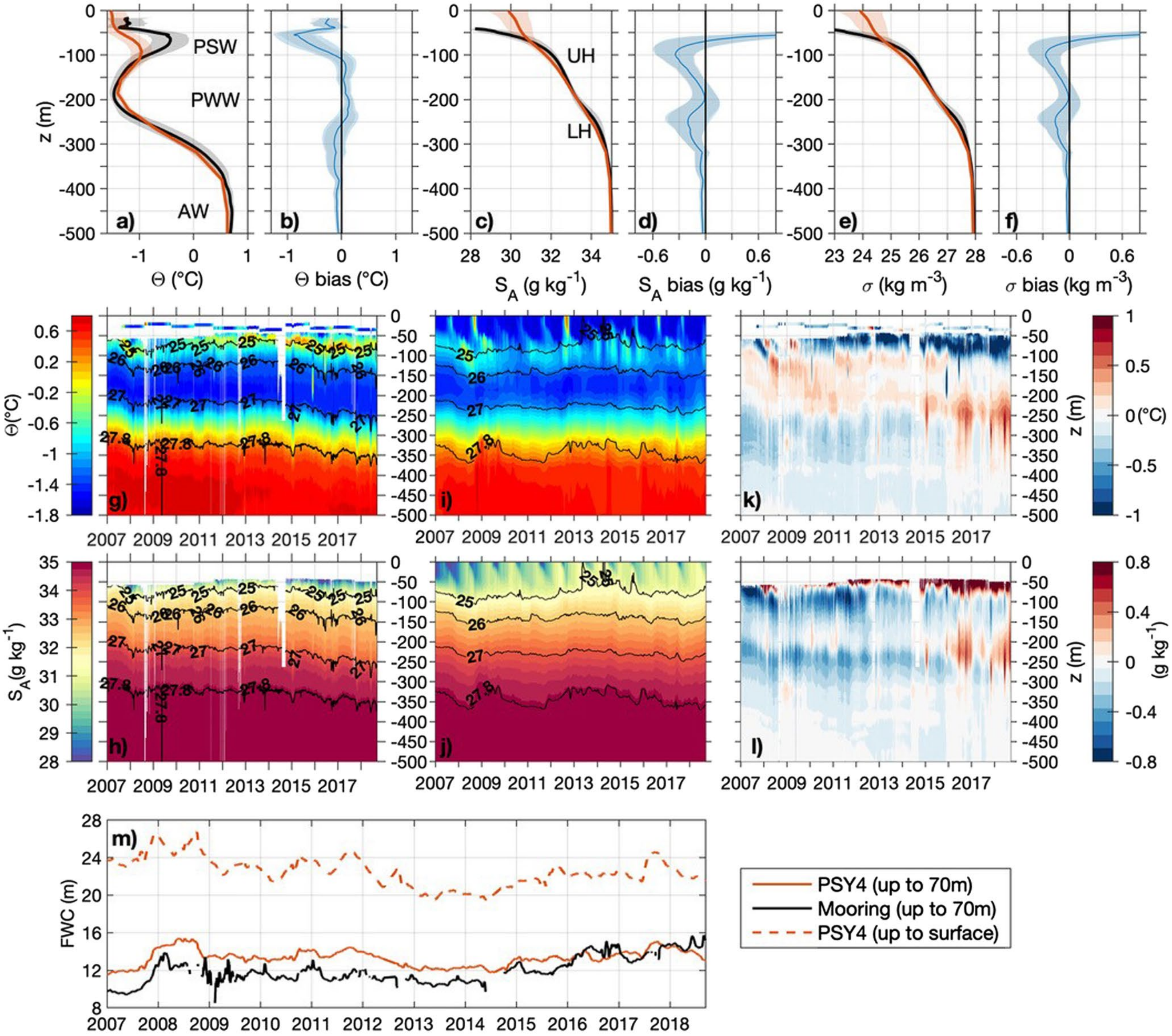

Figure 3. Mean profiles of (a) Θ, (c) S_A, and (e) density σ. Shaded envelopes in gray and light red are standard deviation (STD) around the mean for respectively observations and model. Mean bias profiles of (b) Θ, (d) S_A, and (f) σ. Shaded envelopes are for bias STD (blue) and the sum of model and observations STDs (gray) at each level. Sections of Θ and S_A from mooring D (g–h) and in PSY4 (i–j). Black lines correspond to isopycnals. Differences in Θ and S_A are respectively shown in (k and l). The *x*-axis is time and the *y*-axis is depth. (m) Time series of FWC relative to salinity 34.8 and up to 70 m (plain lines) or the surface (dotted line). *PWW, Pacific Winter Waters; PSW, Pacific Summer Waters; AW, Atlantic Water; UH, Upper Halocline; LH, Lower Halocline.*

3.2. Pacific Waters Inflow Through Bering Strait

We devoted a focused analysis to the capability of the model to simulate the Pacific Water inflow to the Arctic Ocean through the Bering Strait, which is the second main source of freshwater to the Arctic after the continental runoff (Haine et al., 2015). We compare PSY4 to observational mooring data in the Bering Strait. The Bering Strait data come from a centrally located mooring labeled A3 (Figure 4), which has been shown to accurately represent the mean transport and hydrography of Pacific Water inflow to the Arctic through the strait (Woodgate, 2018; Woodgate & Peralta-Ferriz, 2021).

Modeled temperature, salinity, and northward velocities were on average larger than observations with mean yearly biases of +0.38°C, +0.26 g kg^{-1}, and +12.6 cm s^{-1} respectively (Figures 4a–4c). Although PSY4 yearly velocity bias was large throughout the whole time series, it changed little over time (variations of ±1.7 cm s^{-1},

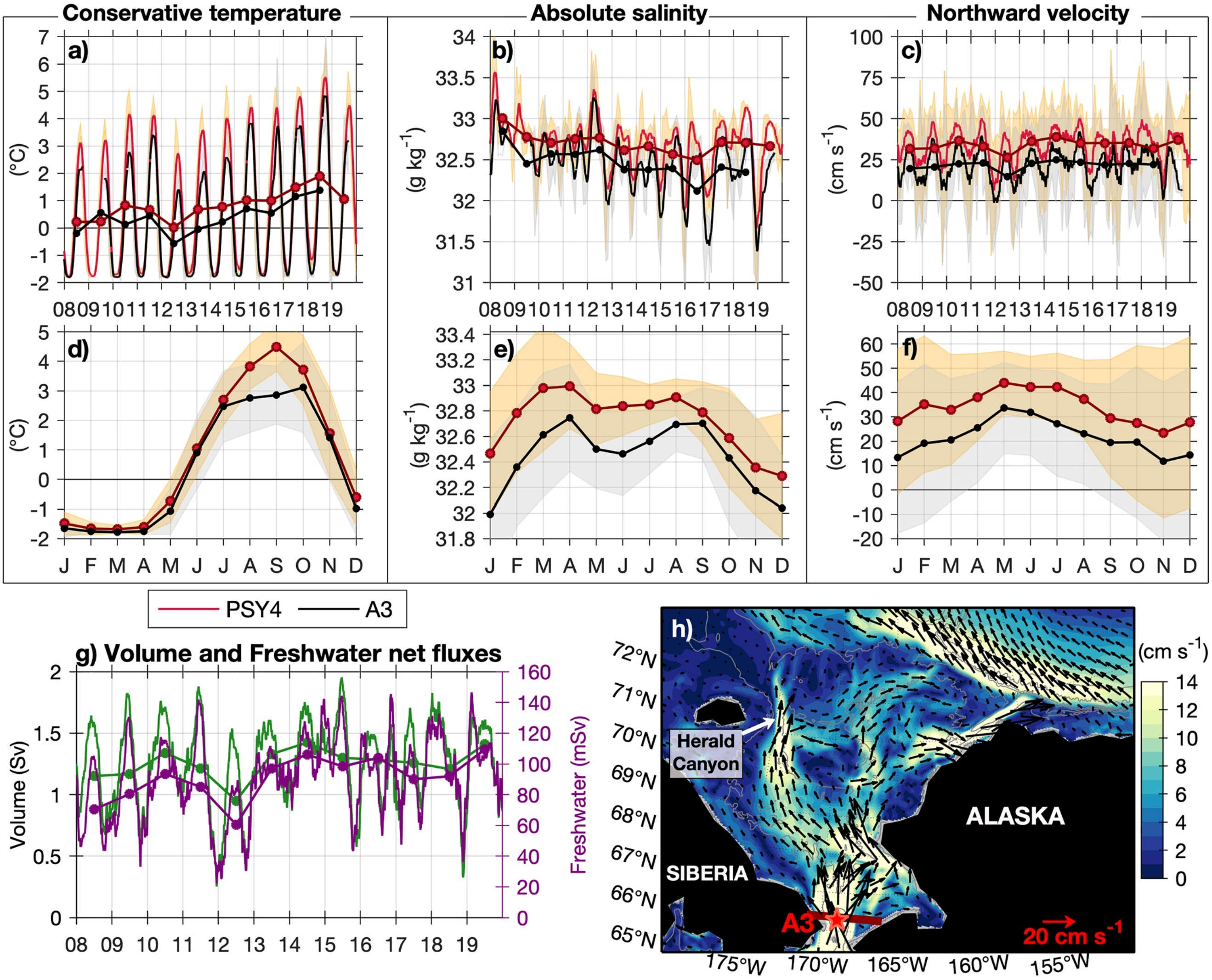

Figure 4. Properties at Bering Strait from mooring A3 data (black) and collocated profile in PSY4 (red). (a, d) Conservative Temperature (Θ; °C) and (b, e) Absolute Salinity (S_A; g kg^{-1}) at 48 m. (c, f) Mean northward velocity at 15–40 m (cm s^{-1}). Shaded envelopes are standard deviations (monthly) for observations (gray) and model outputs (orange). (g) Net fluxes of volume (green, left *y*-axis; in Sv) and freshwater (purple, right *y*-axis; in mSv), positive values being northward fluxes. From (a to g), plain lines and circles correspond to monthly and yearly means respectively. The *x*-axis gives years (2007–2019) or months (first letter of each month). (h) Mean velocities over 2007–2020 in PSY4 at 5 m depth. The mooring A3 position is indicated with a red star.

Figure 4c) and could be considered nearly constant. Interannual variations of modeled temperature, salinity, and northward velocities closely followed that from the observations as quantified by the large correlation coefficients obtained from yearly means ($r^2 = 0.76$, $r^2 = 0.86$, and $r^2 = 0.85$ for temperature, salinity, and northward velocities respectively). The modeled warming in 2012–2019 was in close accordance with the observations (trends of +0.24 and +0.31°C yr^{-1} respectively; Figure 4a). From 2012 onwards, the model reproduced the observed freshening (~ -0.02 g kg^{-1} yr^{-1} in PSY4 and ~ -0.05 g kg^{-1} yr^{-1} in observations). Particular fresh events recorded in winter (impacting PWW), such as in 2013, 2016, and 2019 (Woodgate, 2018; Woodgate & Peralta-Ferriz, 2021), were replicated in the model with a model-observation salinity correlation at $r^2 = 0.87$ in winter (vs. $r^2 = 0.57$ in summer, Figure 4b). PSY4 additionally showed reduced velocities in the winters of 2012, 2016, and 2019 in agreement with observations (Figure 4c).

Seasonal cycles were reproduced well with an overlap of standard deviation envelopes from the model and observations (Figures 4a–4f). During summer (August–September), modeled PSW were too warm ($0.5 < \Delta\Theta < 2$°C, Figure 4d), and too salty ($0.5 < \Delta S_A < 1.3$ g kg^{-1}, Figure 4e). Such a warm and salty summer bias probably resulted from upstream bias in the North Pacific. In contrast, in winter modeled PWW exhibited realistic temper-

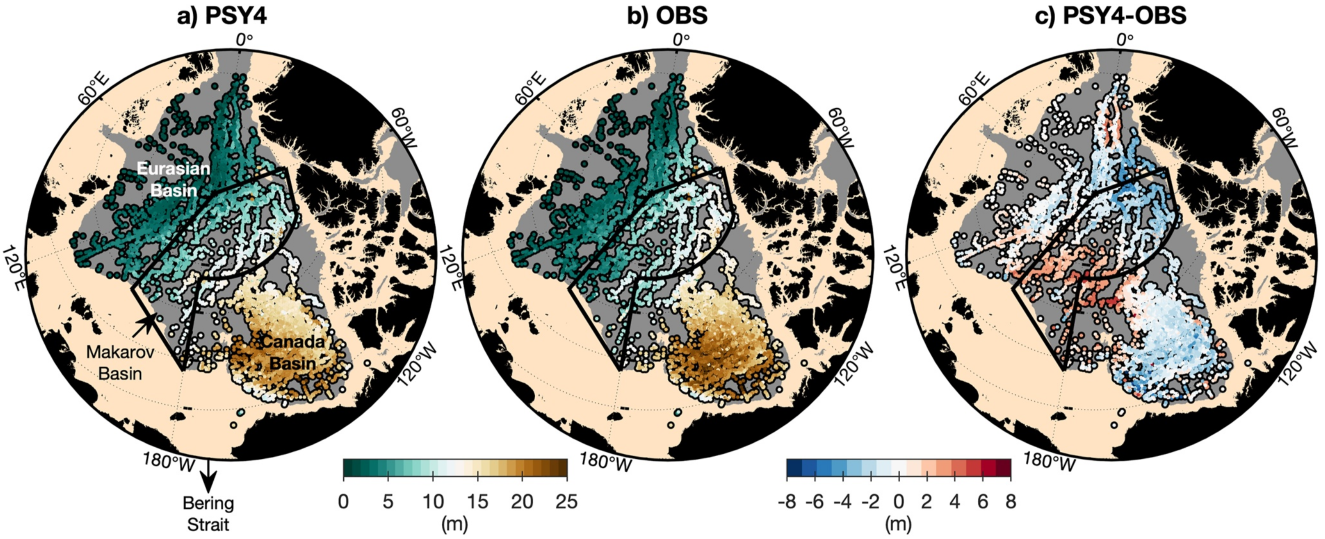

Figure 5. FWC relative to salinity 34.8 psu and computed up to the surface. (a) PSY4 profiles collocated both in space and time with observations. (b) In situ profiles. (c) Model-observation difference. The black box corresponds to the Makarov Basin.

atures ($\Theta \sim -1.8°C$) and salinities ($\Delta S_A < 0.2$ g kg^{-1}, Figures 4d and 4e). Modeled velocities displayed a realistic seasonal signal with larger values in summer than in winter, a maximum in May-June, and a minimum in November, as in the observations (Figure 4f).

The modeled circulation patterns north of the Strait, which shape the distribution of Pacific Waters in the Canada Basin and Makarov Basin, were consistent with observation-based descriptions in the literature (Figure 4h). Indeed, the Pacific inflow split into two branches north of mooring A3 (Spall et al., 2008). One branch circulated northeastward and separated into two parts: one following the Alaska coast and entering the Canada Basin via Barrow Canyon, and another going north in the central Chukchi Sea (Pisareva et al., 2015). The second branch flowed west and exited the Chukchi Sea through Herald Canyon while feeding the central branch of the Chukchi Sea (Corlett & Pickart, 2017; Stabeno et al., 2018).

The modeled net volume flux through the strait averaged over 2008–2019 (~1.3 Sv; 1 Sv = 1 Sverdrup = 10^6 m^3 s^{-1}; green curve in Figure 4g) was a little larger than that found by Woodgate (2018) ($\Delta \sim 0.2$ Sv), likely resulting from the shift of ~13 cm s^{-1} found in modeled velocities. Nevertheless, the mean FWC net transport (~90 mSv, purple curve in Figure 4g) was consistent with that computed by Woodgate (2018) (~95 mSv). Particular observed events, such as smaller transports in 2012 (Woodgate, 2018), were reproduced in PSY4.

3.3. Freshwater Content and SSH

Modeled FWC over the Arctic basins showed a spatial distribution in accordance with the observations, with values lower than 10 m in the Eurasian Basin and 15–30 m in the Makarov and Canada Basins (Figures 5a and 5b). In particular, the modeled and observed FWC were the largest in the BG area, where it is known to have accumulated since the early 2000s compared to pre-1990 climatologies (e.g., Proshutinsky et al., 2009, 2019). Due to the surface salinity bias, PSY4 generally underestimated the FWC (ΔFWC ~ 0–3 m, Figure 5c). Yet, model-observation differences remained smaller than 10% of the mean observed value. This is relatively low, as simulated Arctic FWC can largely vary from one model to the other, in particular in the Canada Basin where values range from 6 to 20 m (c.f. Figure 2 in Jahn et al., 2012; Solomon et al., 2020). We additionally computed the modeled FWC at the mooring location in the BG from the depth of the salinity reference up to 70 m, as the mooring data were only available below 70 m (Figure 3m). In that case, modeled salinity near the surface was not taken into account and the model-observation differences remained on average less than 2 m (15% of the mean observed values) over the entire 2007–2018 period. Improving the surface salinity in the model thus would benefit the modeled FWC.

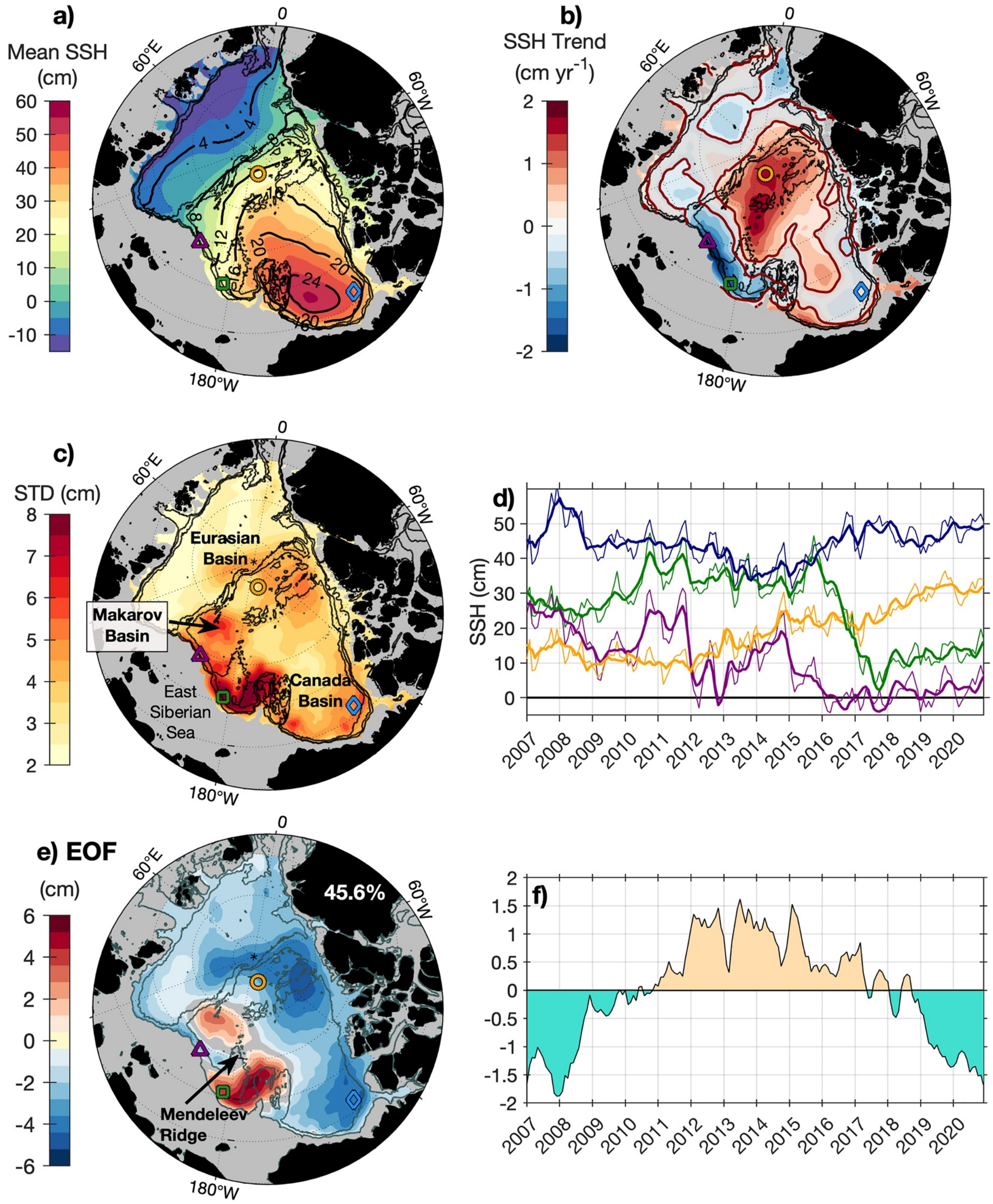

Figure 6. (a) Mean PSY4 SSH (cm) over the 2007–2020 period. Isocontours of mean PSY4 FWC are shown in black. (b) Yearly trends (cm yr^{-1}). Red isocontours delimit areas where trends are significantly larger than the standard deviation. (c) standard deviation from monthly SSH (cm, seasonal cycle removed, detrended field). Time series of (d) SSH (thin lines for monthly means and thick lines with seasonal cycle removed) at four locations indicated with colored circles in (a–c) (*yellow circle: close to the North Pole; purple triangle: along the East Siberian Sea slope; green square: over the Mendeleev Ridge; blue diamond: close to the Beaufort Sea*). (e) SSH EOF1 spatial structure and (f) associated Principal Component.

In the Arctic, spatial patterns of SSH closely follow that of the FWC, with low SSH values in the Eurasian Basin (SSH <10 cm) and large values in the BG (SSH >50 cm, Q. Wang, 2021; Figure 6a). We found that model SSH was in close accordance with the altimetry data (Figure S4 in Supporting Information S1). Model-altimetry SSH differences were on average lower than 12 cm and localized over bathymetric slopes. Significant SSH differences between the model and observations were confined to shelves and the eastern Eurasian Basin while values in the Amerasian Basin (area of interest) remained smaller than 25% (Figure S4 in Supporting Information S1). The large differences in percentage have to be considered with the coarse resolution of the altimetry product in mind. Indeed, the CPOM grid (0.75° × 0.25°) likely does not capture sharp SSH gradients close to the continental shelves.

In summary, the model generally reproduced the observed temperature and salinity in the upper Arctic Ocean. Quantitative comparisons showed that modeled PSW were warmer than observations in the Bering Strait and colder in the Canada Basin, while differences in PWW were small. Pacific Water inflow at Bering Strait was consistent with observations and was associated with a realistic freshwater flux and a slightly overestimated volume flux (Figure 4g). AW in the Eurasian Basin was colder than observations. Overall, the modeled FWC and SSH were in accordance with the observations. In the next section, we examine the interannual evolution of SSH and FWC in the Arctic Ocean.

4. Interannual Evolution of the Arctic Upper Water Column From 2007 to 2020

4.1. Modeled Sea Surface Height Trends and Variations

The SSH is closely related to FWC distribution as illustrated in Figure 6a. However, SSH does not depend on the choice of a reference value, in contrast to FWC. For our analysis, we removed regions over the shelves where SSH variability is much larger than in the basin (e.g., Armitage et al., 2018). We additionally removed the seasonal cycle to only consider interannual variations.

Over the 2007–2020 period, the SSH trends were the largest in the Amerasian Basin with ~+1.5 cm yr^{-1} near the North Pole and ~−1.5 cm yr^{-1} along the slope north of the East Siberian Sea (Figure 6b). In both cases, the 14 years trends were larger than the interannual standard deviation. Furthermore, the monthly variability of SSH was the highest in the southern Mendeleev Ridge (180°E) where the standard deviation exceeded 7 cm (Figure 6c).

Considering these SSH trends and variations, we chose four locations where time series illustrated the dominant interannual variations in SSH (Figure 6d). Two points were taken along the East Siberian Sea where the SSH trend was negative, including one where the standard deviation was large (purple triangle and green square in Figure 6a). The SSH time series along the East Siberian Sea slope showed two local maxima in 2011 and 2014 despite the overall decrease (purple line, Figure 6d). South of the Mendeleev Ridge (green square in Figure 6a), SSH increased until reaching a plateau from 2011 to 2016 (SSH ~ 38 cm, green line, Figure 6d). Hence, the negative linear trend at this location resulted from the sharp step in 2016–2017 (ΔSSH ~ 35 cm).

In the Beaufort Sea, SSH diminished during the 2011–2014 period (blue diamond and blue line in Figures 6a–6d). This was consistent with the shift of the BG toward the Mendeleev Ridge described by Regan et al. (2019). Interestingly, the SSH over the Beaufort Sea gradually increased after 2014, suggesting a return of the gyre extension to the east (blue line in Figure 6d). In contrast, SSH gradually increased near the North Pole after 2012, from 10 cm to nearly 30 cm in 2020 (yellow line in Figure 6d), in accordance with the strong positive trend of +1.5 cm yr^{-1}.

Interannual variations of SSH were further examined using an Empirical Orthogonal Function (EOF) analysis, after detrending and removing the seasonal cycle from the data. The leading mode (EOF1, Figure 6e), explaining 45.6% of the variance, featured opposite sign patterns with positive SSH anomalies on the western part of the Amerasian Basin (~4 cm) and negative SSH anomalies on the eastern part of the basin (~−4 cm). The associated time series exhibited low-frequency variations (Figure 6f). During 2011–2017, the EOF analysis suggested an increase of SSH in the west that can be interpreted as a western extension of the BG toward the Chukchi Plateau (Regan et al., 2019, 2020). Before 2010 and after 2018, as the Principal Component was negative, there was a decrease in SSH over the Mendeleev Ridge combined with an increase on the Beaufort Sea and north of the Canadian Archipelago. This simultaneous eastward and a northward shift of large SSH values suggested substantial variations of the BG, which we further examine in the following.

4.2. Focus on the Amerasian Basin

4.2.1. Evolution of the Beaufort Gyre From Model Sea Surface Height

Following Regan et al. (2019, 2020), the center of the gyre was defined as the maximum SSH (hereafter $\mathrm{SSH}_{\mathrm{max}}$) located in a box 190°–230°E, 70.5°–80.5°N. The limit of the gyre was taken as the largest closed

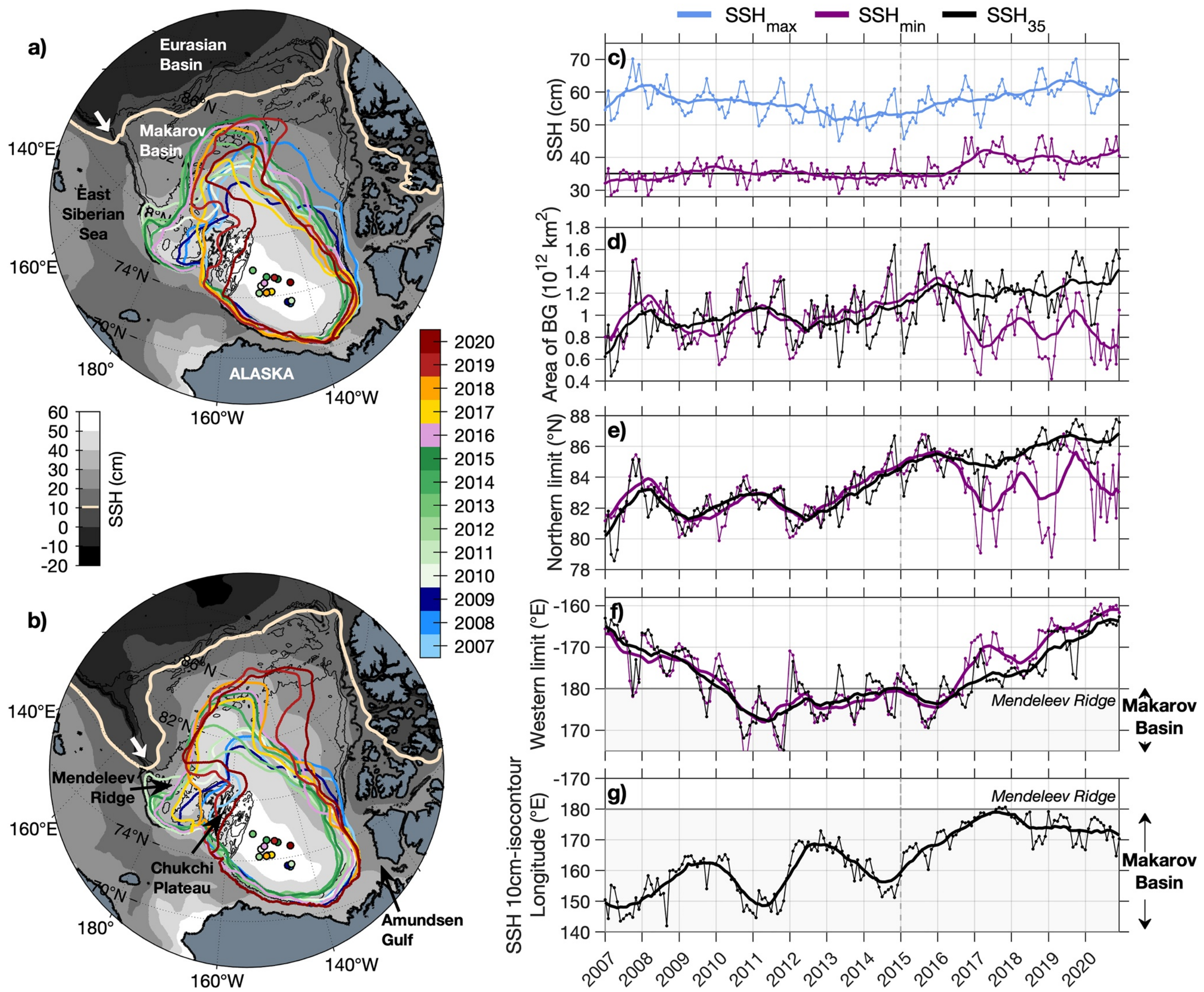

Figure 7. (a) Yearly mean SSH isocontours of the Beaufort Gyre limit from 2007 to 2020 following Regan et al. (2019). Centers of the Beaufort Gyre determined from the location of SSH_{max} are indicated for each year. The background color is the SSH field in 2011 and the isocontour SSH = 10 cm is shown in beige. Black isocontours in the background indicate IBCAO bathymetry 2,000, 1,000, and 500 m (thick black line). (b) same as (a) with Beaufort Gyre limit obtained from SSH isocontour 35 cm. Background color is the SSH field in 2016. (c) SSH_{max} corresponding to the Beaufort Gyre center (blue) and SSH_{min} corresponding to the BG limit in (a) (purple). The black line is for SSH = 35 cm. (d) Area of the Beaufort Gyre computed in Figures 11a (purple) or 11b (black). (e) Northern limit (°N) of the Beaufort Gyre using SSH_{min} (purple) or 35 cm SSH isocontour (black). (f) Western limit (°E) of the Beaufort Gyre using SSH_{min} (purple) or 35 cm SSH isocontour (black). (g) Longitude of the easternmost point of SSH 10 cm isocontour indicated by the white arrow on (a and b). From (c to g), thin lines are monthly means and thick lines are for 12-month running mean.

SSH isocontour (hereafter SSH_{min}) surrounding the center. We considered that the selected SSH isocontour should not cover any plateaus shallower than 250 m, to discard closed isocontours entering the Amundsen Gulf. The gyre center and limit derived from PSY4 (Figures 7a and 7c) were similar to those derived from altimetry data over 2007–2014, the period used in Regan et al. (2019). The SSH_{max} exhibited a minimum in 2014. The SSHmin notably increased in 2016 from persistent values of around 35 cm between 2007 and 2015 to around 40 cm from 2017 to 2020. The increase of SSH_{min} in 2016 was accompanied by a large decrease of the gyre area from a maximum of 1.3×10^{12} km^2 at the end of 2015 to 0.75×10^{12} km^2 at the beginning of 2017.

From 2016 onwards, large SSH values on the shelves off Alaska (SSH ≥35 cm, c.f. positive trend over the shelves in Figure 6b) led to isocontour breakup in this area. We tentatively considered the 35 cm SSH isocontour (hereafter SSH_{35}) as the limit of the gyre (purple line in Figure 7c) and closed it along the 500 m isobath. The interannual variations of the SSH_{35} differed from those in Regan et al. (2019) method after 2016. In particular, the BG area using SSH_{35} remained large, with 1.3×10^{12} km^2 (Figures 7a–7d).

Using both methods, the northern limit of the BG shifted discernibly from 81°N to 86°N in 2016 (Figure 7e), with an associated SSH increase near the North Pole (Section 4.1 and Figure 6d, yellow line). After 2016, the SSH_{35}-derived northern limit continued its progression until 87°N, while the limit derived from SSH_{min} returned southward, leading to the difference in BG areas (Figures 7d and 7e).

The western limit of the BG (i.e., boundary location with the smallest longitude and latitude) was similar following both methods. The BG western limit was located between the western Chukchi Plateau and Mendeleev Ridge (~170°W–180°E) from 2007 to 2009 (Figure 7f). From 2010 to 2016, the limit extended over the Mendeleev Ridge (~170°E−180°E). This is consistent with the westward extension of the gyre described by Regan et al. (2019) and explains the SSH plateau found in the area (Section 4.1. and green line, Figure 6d). Eventually, the gyre moved back eastward after 2016, inducing the increase of SSH near the Beaufort Sea described in Section 4.1 (blue line in Figure 6d).

4.2.2. Freshwater Content Increase in the Central Makarov Basin

The progressive increase in SSH near the North Pole associated with BG migration suggests a related change in FWC in the Makarov Basin. From 2010 to 2011 the BG was skewed to the southwest and its north limit was south of 83°N. During this time, FWC north of the gyre in the Makarov Basin decreased from 16 m close to the Mendeleev-Alpha Ridge to 6 m near the Lomonosov Ridge (Figure 8a). The Hovmöller diagram along a section crossing the Makarov Basin showed that the FWC increased near the North Pole (horizontal plain line in Figure 8d) from ~11 m in 2012 to ~ 17 m in 2018. Indeed, from 2014 to 2015 the BG boundaries penetrated the Makarov Basin via the Mendeleev-Alpha Ridge junction (Figure 8b). Coincidently, the halocline deepened by about 50 m between the 2007–2011 and 2016–2020 periods, inducing a negative salinity difference centered at 100 m depth of -1.3 g kg^{-1} (Figure 9). In 2019–2020, the contours of the gyre extended northward, and a new secondary reservoir of FWC emerged along the southern flank of the Mendeleev-Alpha Ridge (FWC ~ 21 m, Figure 8c). The emergence of this new reservoir of FWC contributed to extending the BG limit northward (when defined by SSH_{35}).

This spatial redistribution of FWC was accompanied by an Arctic-wide increase in FWC (Figure 8e). The annual average of the modeled freshwater volume calculated over the deep basins (bathymetry >500 m) increased from a minimum of 53,000 km^3 in 2013 to a maximum of 60,000 km^3 in 2020. Note that values of annual freshwater volume from PSY4 and before 2013 are comparable to the annual freshwater volume of about 50,000 km^3 computed in Rabe et al. (2014) over the 2007–2012 period. PSY4 values suggested that this Arctic-wide modeled freshwater volume increase resulted essentially from the accumulation of freshwater in the Amerasian Basin (green and black curves in Figure 8e).

4.2.3. Progressive AW Shoaling Along the East Siberian Sea Slope

Another striking feature was the reduction of the SSH along the northern edge of the East Siberian Sea described in Section 4.1. The SSH fields averaged over 2011 and 2016 are shown in the background of the maps in Figures 7a and 7b, respectively. In 2016, the 10 cm iso-contour delineated a region with low SSH encroaching the Makarov Basin along the East Siberian Sea slope. Such low SSH (<10 cm), comparable to values encountered in the Eurasian Basin, likely delineated denser waters of Eurasian origin. The longitude of the 10 cm iso-contour easternmost position in the area of the slope (white arrow in Figure 7a) has increased from 160°E in 2011 to a maximum of 180°E in 2017, exceeding 150°E after 2014 permanently (Figure 7g). Accordingly, the FWC decreased along the northern border of the East Siberian Sea after 2012 to less than 8 m (position ~200 km of the section in Figure 8d). This reduction in FWC resulted from a shoaling of isohalines by about 50 m near the continental slope (Figures 9a and 9b), inducing a large positive salinity difference in the upper 150 m (+1.7 g kg^{-1}, Figure 9) between the 2007–2011 and 2016–2020 periods. This is consistent with a shoaling of the warm, salty AW as a result of Atlantification (e.g., Polyakov et al., 2017, Polyakov, Rippeth, et al., 2020).

In summary, the modeled SSH evolution (driven by FWC variations via the halosteric effect) documented three major changes in the central Arctic since 2007. The BG extended westward from 2011 to 2016 and then retreated

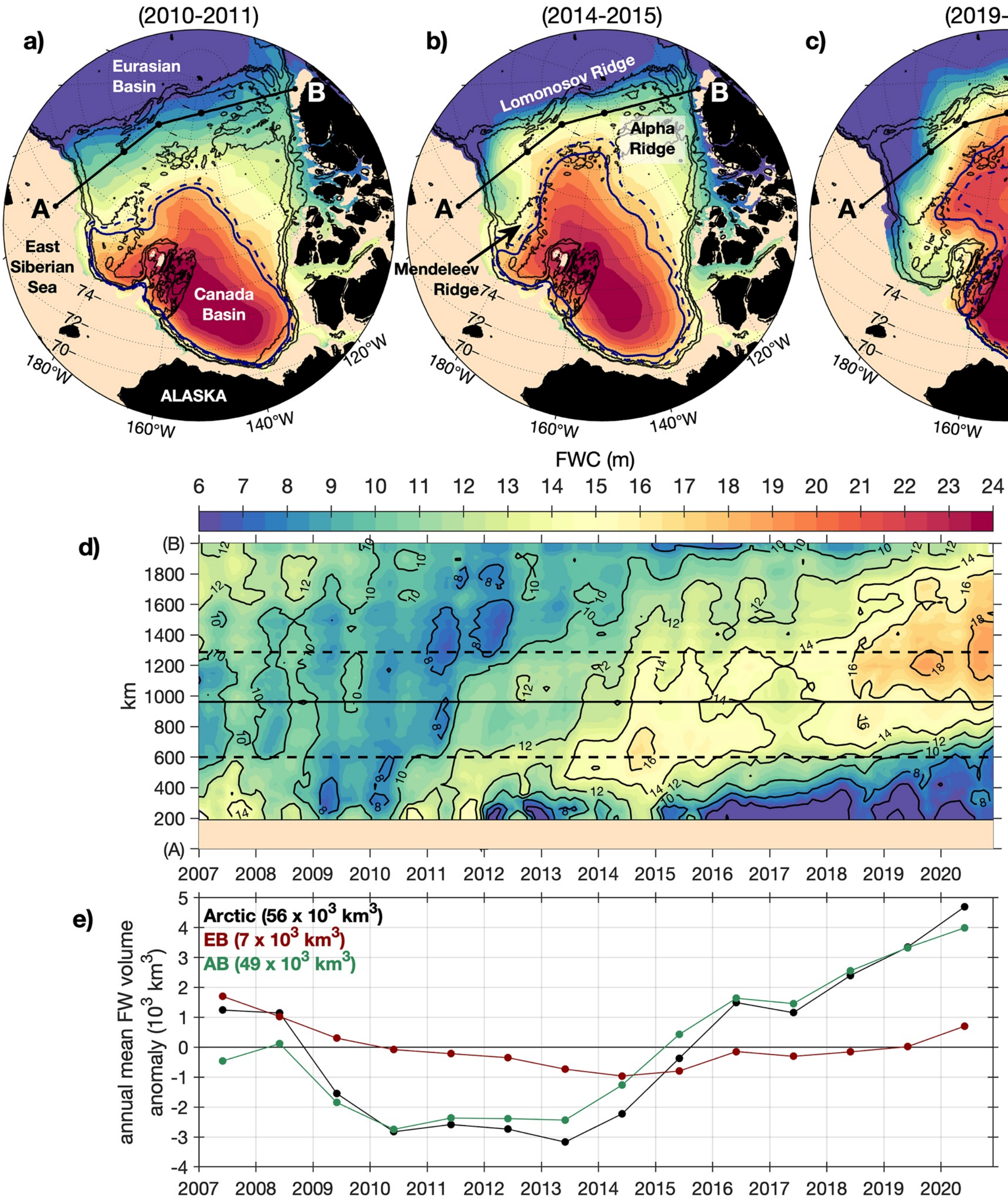

Figure 8. Freshwater content (FWC) relative to $S_{\mathrm{ref}} = 34.8$ psu in the deep basin (bathymetry >300 m) averaged over 2 years period (a) 2010–2011, (b) 2014–2015 and (c) 2019–2020. Plain and dashed contours are for BG limits using SSH_{35} or $\mathrm{SSH}_{\mathrm{min}}$ respectively in 2011, 2015, and 2020. Colorbar is the same as panel (d). (d) Hovmoller of the monthly FWC along a section across Makarov Basin. The thin black line separates the Siberian side from the eastern side of the basin and corresponds to the black dot in the middle of the section on maps. Dashed lines correspond to the two other black dots of the section. (e) Yearly freshwater (FW) volume anomalies over deep basins ("Arctic" in black; bathymetry >500 m), Eurasian Basin (EB; red), and Amerasian Basin (AB; green). The mean freshwater volume over the 2007–2020 period is given above the panel.

eastward. Near the North Pole, the SSH (and thus FWC) began to increase from 2012 as the BG extended northward. In parallel, the FWC decreased after 2012 along the East Siberian Sea slope, due to the progressive shoaling of AW. Modeled ocean circulation, freshwater pathways, and outflows from the Arctic are examined in the following section.

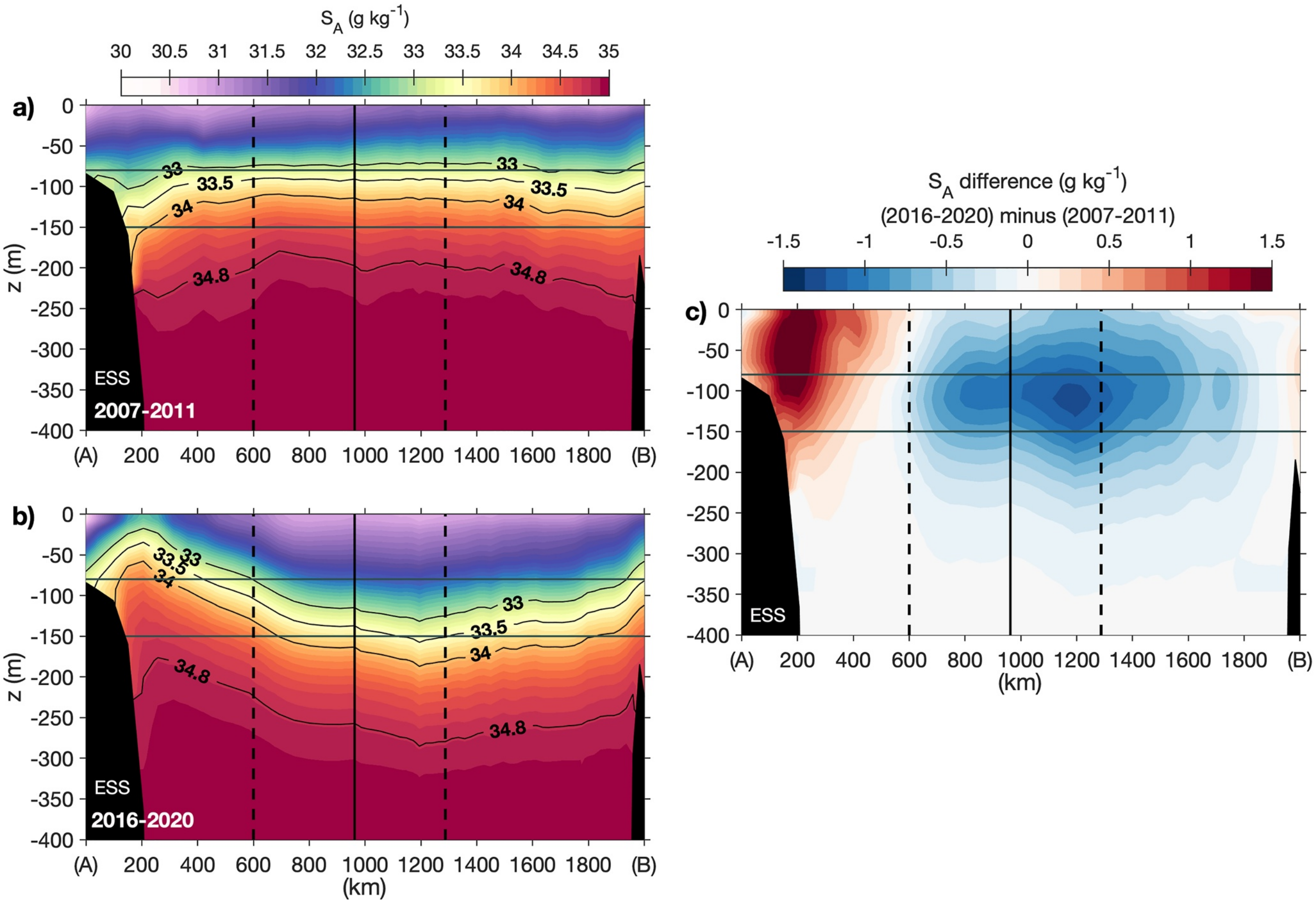

Figure 9. Absolute Salinity S_A (g kg^{-1}) averaged over the (a) 2007–2011 and (b) 2016–2020 periods along the same section in the Makarov Basin already shown in Figure 8. The x-axis is the distance (km) starting from ESS. Horizontal black lines indicate 80 and 150 m depth to ease the reading. The vertical black line separates the Siberian part from the central part of the basin. (c) S_A difference between the two periods along the section (g kg^{-1}).

4.3. Recent Changes in the Upper Layer Ocean Circulation and Freshwater Pathways

4.3.1. Large-Scale Changes in Ocean Circulation

To illustrate large-scale changes in upper ocean circulation, we averaged horizontal velocity fields over different periods: 2007–2020, 2010–2011, 2014–2015, and 2019–2020 (Figure 10). The 2007–2020 mean modeled ocean circulation in the upper water column was consistent with the descriptions found in the literature (Figure 10a). The westward current larger than 9 cm s^{-1} south of the BG corresponded to the Chukchi slope current described by Corlett and Pickart (2017). The modeled TPD was on average confined over the Makarov Basin (Figure 10a, see e.g., Karcher et al., 2012; Kwok et al., 2013; Timmermans & Marshall, 2020). The mean anticyclonic surface circulation in the Canada Basin, corresponding to the BG, was associated with surface velocities smaller than 3 cm s^{-1} as in Armitage et al. (2017).

The Chukchi Slope Current, which reached the western part of Mendeleev Ridge in 2010–2011 (Figure 10b), retreated to the eastern part of the Chukchi plateau in 2019–2020 (Figure 10d). In parallel, the boundary current north of the Laptev Sea, previously not extending beyond the Lomonosov Ridge, reached the Mendeleev Ridge in 2019–2020 (Figure 10). The circulation branch over the Makarov Basin in 2010–2011 and 2014–2015 was likely fed either by the BG, via the Chukchi Slope Current, or by waters from the Laptev Sea and the Eurasian Basin (Figures 10b and 10c). The upper water column velocities suggested that the TPD intensified from 2010 to 2011 ($v_{80m} \sim 2.5$ cm s^{-1}) to 2014–2015 ($v_{80m} > 5$ cm s^{-1}) and shifted from the Lomonosov Ridge in 2014–2015 to the Mendeleev Ridge in 2019–2020. Velocities in the southern part

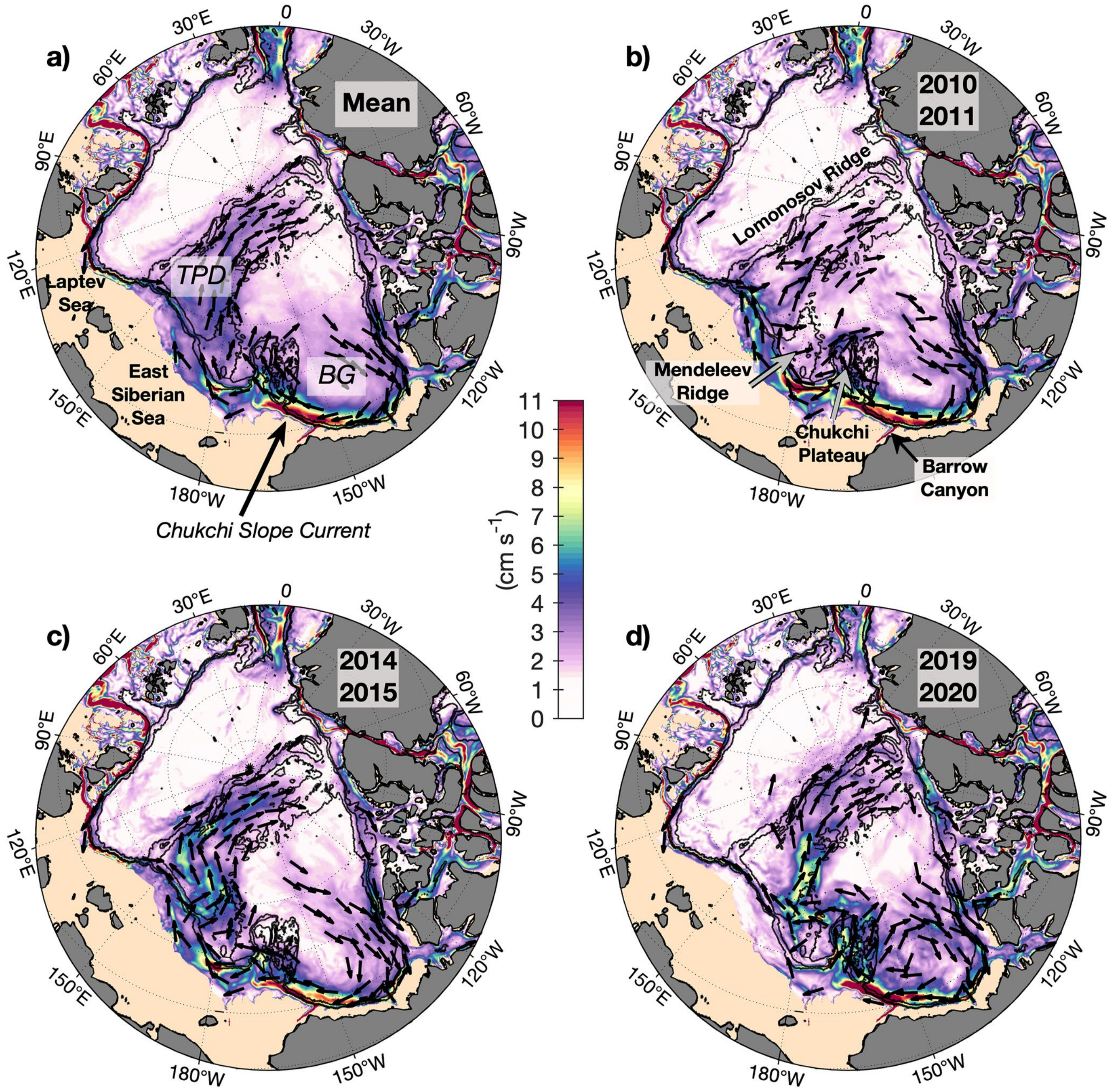

Figure 10. Ocean velocities at 80 m averaged over (a) the 2007–2020 period and the 2 years periods (b) 2010–2011, (c) 2014–2015, and (d) 2019–2020. For clarity, normalized velocity vectors are shown only in the Amerasian Basin and if velocity intensity is larger than 2 cm s^{-1} and velocity vectors over the Barents Sea were removed. *TPD, Transpolar Drift; BG, Beaufort Gyre*.

of the Canada Basin also intensified in 2019–2020 compared to 2014–2015 (around 140°W near Barrow Canyon, Figures 10b and 10c).

4.3.2. Freshwater Routes in the Canada and Makarov Basins

We further illustrated BG changes by following particles initially located in the gyre center with the particle tracking method described in Section 2.2. We released particles in a box spanning the region 72°–79°N, 170°W–130°W at various depths and different seasons (one launch at the end of the winter and the other at the end of the summer) and tracked their trajectories for 6 years (the first 3 years at 80 m shown in Figures 11a and 11b). Particles

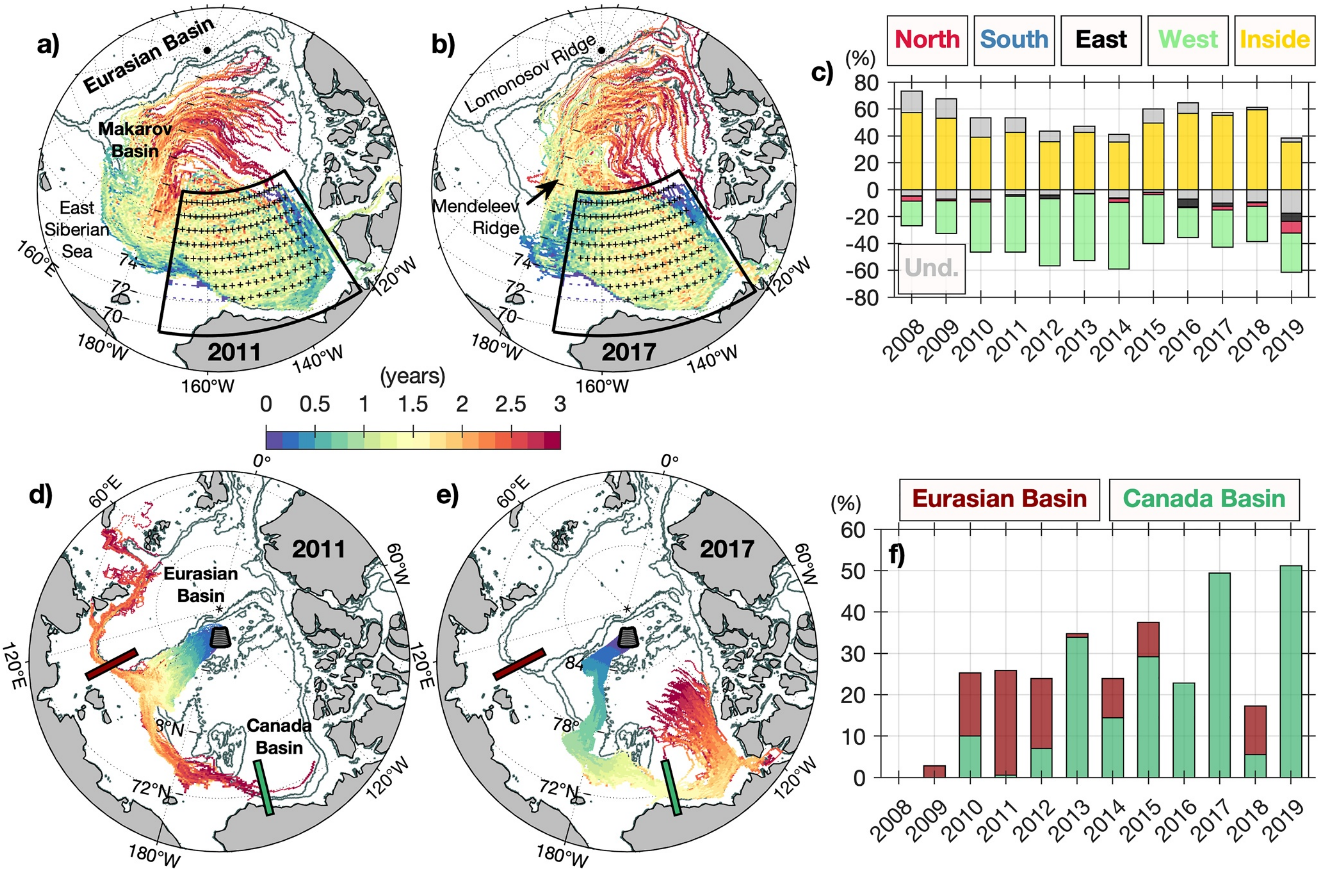

Figure 11. Trajectories calculated with PSY4 daily horizontal velocities fields at 80 m (Color is the time from launch). See Section 2.2 for the method. (a–b) Forward trajectories of particles launched in the Beaufort Gyre in (a) 2011 and (b) 2017. (c) Percentage of particles entering and leaving for each side of the Beaufort Gyre box (shown in (a–b)) as a function of launching year, negative values corresponding to the outputs (*South: blue; West: green; North: red; East: black*). *Inside (yellow)* corresponds to particles that never leave the box. *Und (gray)* corresponds to particles that exit and enter several times during their trajectory. (d–e) Backward trajectories of particles from the central Makarov Basin launched in (d) 2011 and (e) 2017. (f) Percentage of particles from the central Makarov Basin passing through the Eurasian Basin (red) or Canada Basin (green) gateways during the 3 years preceding the launch (launch year on the *x*-axis).

released in the BG box upper layer first circulated anti-cyclonically in the Canada Basin, before exiting the gyre and ending their course in the central Makarov Basin (Figures 11a and 11b). From 2008 onwards, the main exit gate was to the west of the gyre, which is consistent with Hu et al. (2019). However, there was a change in the particle paths. Before 2015, particles that exited the BG flowed westward along the East Siberian Sea slope, and then entered the deep Makarov between 155°E and 175°E (e.g., 2011 shown in Figure 11a). There was an increase in westbound exits until 2014 (~10% in 2008 to more than 30% in 2014, green bars in Figure 11c), while the percentage of particles remaining inside the BG box decreased from ~60% in 2008 to ~35% in 2014 (yellow bars in Figure 11c). After 2015, more particles exited the gyre from the north (less than 5% in 2014 and ~10% in 2017, red bars in Figure 11c) and less from the west (~15% in 2017, Figures 11b and 11c), while about 40%–60% of the particles remained inside the BG box. This is consistent with the northward shift of the BG and the eastward shift of the TPD: the particles leaving the gyre to the west progressed directly northward, along the Mendeleev Ridge at 180°W into the TPD (Figure 11b). Such changes in freshwater routes in the Amerasian Basin are in accordance with the increase of FWC near the North Pole after 2014 (Figure 8d).

Additionally, changes in freshwater routes in the Amerasian Basin were investigated using back-trajectories from the central Makarov Basin (86.5°–88°N; 150°W–175°W) where the FWC increase was maximum. Particles were released at various depths and starting times (level 80 m shown in Figures 11d and 11e for sake of illustration). Back-trajectories over the 2010–2012 period showed larger contributions from the Eurasian Basin (>15%, Figures 11d and 11f) than the Canada Basin (<10%), with an additional contribution from the Laptev Sea near the surface (not shown). Sources and pathways changed after 2012 over the entire upper 150 m, with major

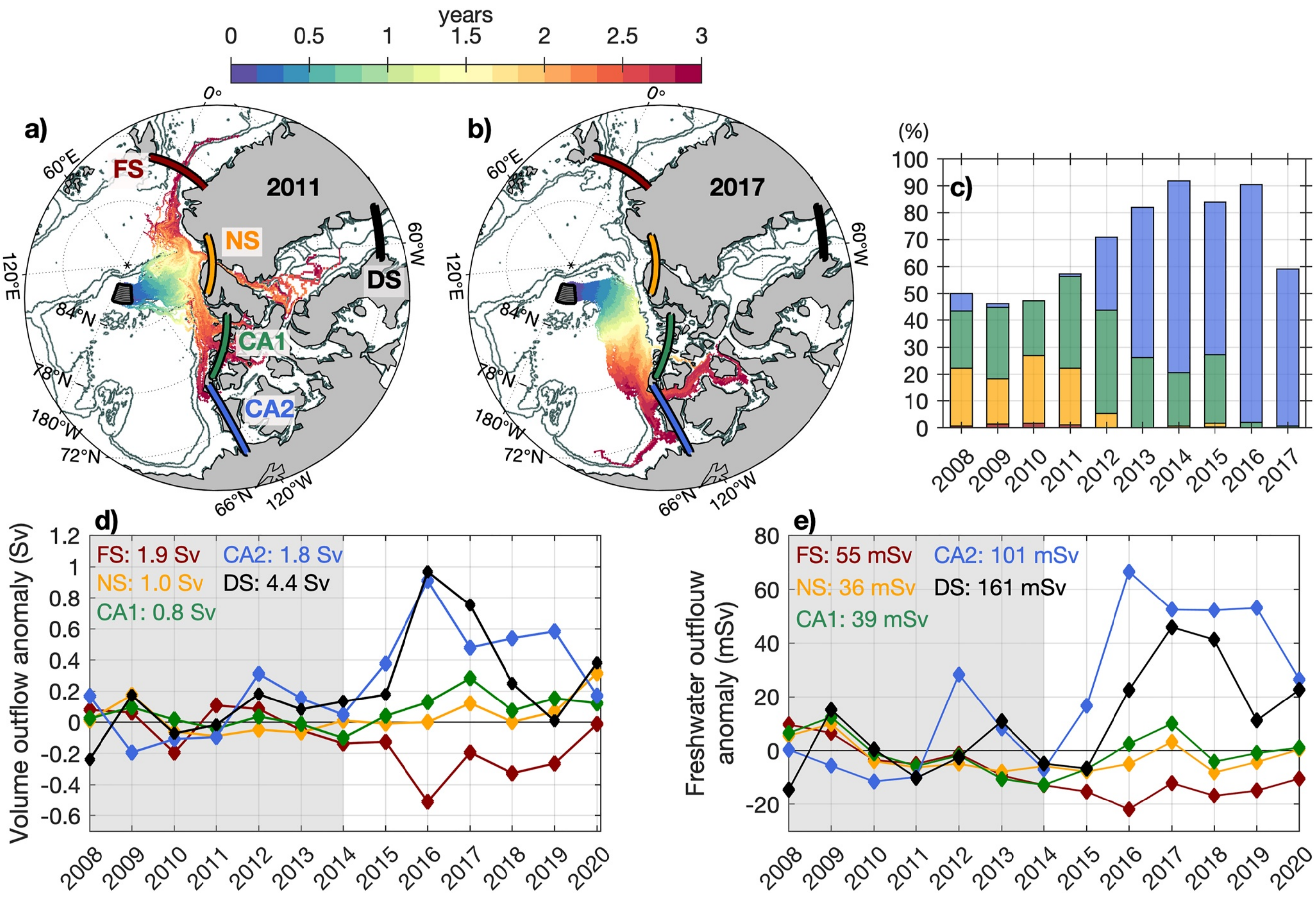

Figure 12. Forward trajectories in central Makarov Basin launched at 80 m in (a) 2011 and (b) 2017. Gates are shown in color: Fram Strait (FS, red line), Nares Strait (NS, yellow), CA1 (green), CA2 (blue), and Davis Strait (DS, black). (c) Percentage of particles leaving the Arctic during the 3 years following the launch (*x*-axis). Color corresponds to the gates (FS, NS, CA1, and CA2 only) shown in (a). Yearly anomalies relative to the 2008–2014 period (shaded in gray) of (d) volume outflow (Sv) and (e) freshwater outflow (mSv; reference 34.8 psu) through the gates (mean values over 2008–2014 indicated in color). See Section 2.2 for the method.

contributions coming from the BG (<10% in the Eurasian Basin and> 20% in the Canada Basin, except in 2014 and 2018, Figure 11f). In 2018, the distribution of water parcels coming from the Canada and Eurasian Basins has a very similar ratio to 2010 and 2012, and further work would be needed to examine the involved processes.

The advection of particles from the BG to the Makarov Basin interior has accelerated between 2008 and 2019, as a result of the increasing upper-ocean velocities (Figure 10). The advection time between the two basins was about 2.5 years in 2011, against 1.5 years in 2017 (Figures 11a and 11b and 11d–11e). This could imply that low-salinity waters from the gyre would be less subject to modifications along their course to the Makarov Basin, and further supports our hypothesis of an increased water supply from the BG toward the central Makarov Basin, raising the FWC there.

4.3.3. Freshwater Outflow From the Arctic Ocean

We further illustrated changes in the freshwater pathways out of the Amerasian Basin by performing forward trajectories from the center of the Makarov Basin (level 80 m in 2011 and 2017 shown in Figures 12a and 12b). We quantified exits of the particles within the 3 years after the launch, through the following four gateways: the Fram Strait, the Nares Strait, and the eastern and western part of the Canadian Archipelago (hereafter CA1 and CA2).

Before 2012, the BG had not yet extended toward the North Pole and particles released in the center of the Makarov Basin exited the Arctic via the Nares Strait (~20% at 80 m, yellow gate in Figures 12a and 12c) and CA1 (~30%, green gate) instead of Fram Strait (~3%) or CA2 (~4%). Exit pathways changed after 2012, with particles increasingly leaving the Arctic through CA2 (~40%–80%, blue gate) instead of Fram Strait, Nares Strait, or CA1 (Figures 12b and 12c). This is in accordance with the extended anticyclonic circulation over the Amerasian Basin resulting from BG changes and contributing to transport particles near CA2 (Figure 12b). Trajectories also showed that particles reached gateways faster over the years: about 2–3 years were needed in 2017 instead of ~ 3–4 years in 2011 (Figures 12a and 12b, the color of the trajectories is time).

To quantify freshwater exits from the whole Arctic toward the North Atlantic, we computed volume and freshwater outflows (i.e., southward only) at the four gateways, as described in Section 2.2. We considered anomalies relative to the 2008–2014 period to document the interannual changes (Figures 12d and 12e). Mean outflow values over the early period (2008–2014), indicated in Figures 12d and 12e, were comparable to those found in the literature (see Z. Wang et al., 2017, their Table A1). Unsurprisingly, PSY4 freshwater outflows over 2008–2014 at Fram and Nares Straits (55 and 36 mSv respectively) were on average smaller than values from Z. Wang et al. (2017), likely resulting from the surface salinity bias described in Section 3. Volume and freshwater mean outflows over 2008–2014 at Davis Strait (4.4 Sv and 161 mSv respectively) were larger when compared to 2004–2005 observations from Curry et al. (2011) (Δ ~ 2 Sv and 50 mSv, respectively).

Both volume and freshwater outflow anomalies over 2016–2019 were large through CA2 relative to 2008–2014 (~+0.8 Sv and +65 mSv, respectively) and downstream through Davis Strait (~+0.5 Sv and +30 mSv). In contrast, volume and freshwater outflow anomalies at Fram Strait were smaller over the 2016–2019 period (~−0.5 Sv and −20 mSv, respectively). The interannual evolution of the volume outflow at CA2 was similar to that of the freshwater outflow, implying that part of the freshwater outflow increase resulted from larger volume transport through the gates (blue curve in Figures 12d and 12e). The ratio between the freshwater and volume outflows supported that the 2016 anomaly was also associated with fresher waters exiting through CA2. Peaks of volume outflow anomalies through CA2 and the Davis Strait in 2016 were concomitant, while freshwater outflow anomalies at the Davis Strait lagged CA2 by 1 year (blue and black curves in Figures 12d and 12e).

In summary, trajectories illustrated that freshwater leaking from the BG fed the Makarov Basin following a more direct route from 2012 onwards, which is consistent with the FWC increase in the Makarov and North Pole region. Furthermore, outflows at the exit gateways supported a larger freshwater export through the western Canadian Archipelago rather than through Fram Strait after 2015. The total volume outflow slightly increased by 7% between 2008 and 2014 (mean of 5.5 Sv) and 2015–2020 (mean of 5.9 Sv), resulting from a decrease of 11% (from 1.9 to 1.7 Sv) at Fram Strait and an increase of 15% (from 3.6 to 4.2 Sv) at the Canadian Archipelago (Nares Strait, CA1 and CA2). Although the change in the total freshwater outflow from the Arctic toward the North Atlantic was rather small (+7.5%, from 230 to 248 mSv), the freshwater outflow at Fram Strait decreased by 30% (from 54 to 40 mSv) while the freshwater outflow at the Canadian Archipelago increased by 16% (from 176 to 207 mSv).

5. Discussion

We evaluated the Mercator Ocean operational physical high-resolution system PSY4 over the entire Arctic Ocean, following the satisfactory assessments performed in the western Arctic Eurasian Basin (e.g., Athanase et al., 2021, 2020, 2019). Salinity biases were generally low, except in the upper 100 m in the Amerasian Basin, as it is often the case in numerical models (e.g., Lique et al., 2016; Regan et al., 2020; Q. Wang, Ilicak, et al., 2016). A comparison between the initialization fields in October 2006 and in situ measurements during the same period showed that the initial condition near the surface layer was already too salty (Figure S3 in Supporting Information S1). Improving the initial state might contribute to reducing such biases. Moreover, wind-forced redirection of river discharge played a key role in the freshwater accumulation in the BG area (Proshutinsky et al., 2019) and further studies on PSY4 river inputs to the Arctic Basin may help in understanding their possible contribution to surface salinity biases.

At the Fram Strait gateway, AW entering the Arctic was found in good agreement with observations (Athanase et al., 2020). We additionally showed that PSY4 represents realistic Pacific Water hydrographic properties in the Bering Strait when compared to sustained mooring data (Woodgate & Peralta-Ferriz, 2021). Modeled volume and freshwater fluxes at the strait were close to the observation. The cold PWW was in good agreement with observations. We found that modeled AW in the Eurasian Basin and PSW in the Canada Basin were both colder than observations. PSY4 evaluation over the continental shelf such as Barents, Laptev, East Siberian, Chukchi, or Beaufort Seas, was beyond the scope of this study, and these areas would need particular attention in future

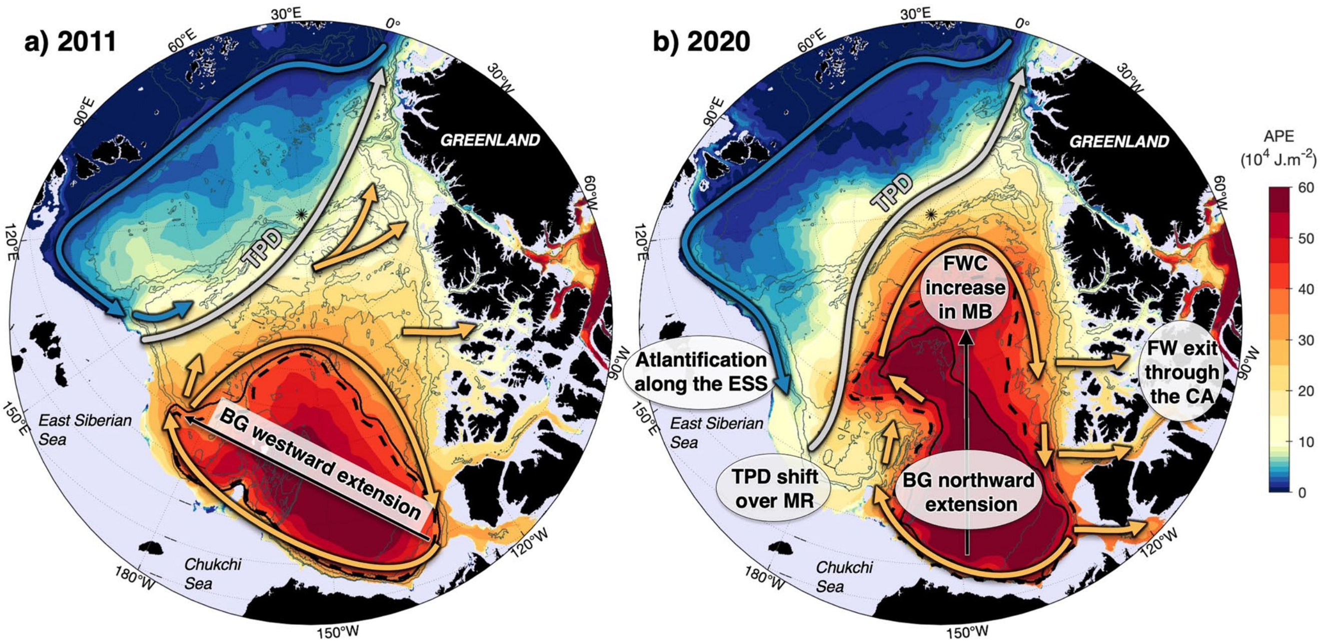

Figure 13. Annual mean model halocline strength in (a) 2011 and (b) 2020 measured with the Available Potential Energy (APE). Schematics arrows highlight major circulation changes (AW in blue and freshwater in orange). Plain and dashed black lines respectively indicate Beaufort Gyre (BG) limits from Regan et al. (2019) criterion and SSH isocontour 35 cm. Before 2012, the BG extended to the west, over Mendeleev Ridge. After 2012, the BG extended northward (yellow arrows) and dense AW shoaled along the East Siberian Sea (ESS) slope (blue arrows). Hence, the freshwater content (FWC) increased in the central Makarov Basin (MB) while it decreased in the Siberian part of the basin. The Transpolar Drift (TPD, in gray arrows) shifted toward Mendeleev Ridge (MR).

studies as local shelf processes, such as winter convection, atmosphere-ocean heat exchanges or sea ice melting, are important (e.g., Athanase et al., 2020; Lind et al., 2018; Rudels et al., 2015). The large-scale distribution of SSH was consistent with the Armitage et al. (2017) remotely sensed altimetry observations, and FWC in PSY4 was congruent to the rather scarce in situ observations in the Arctic Ocean or the mooring data in the Canada Basin (Proshutinsky et al., 2009).

The Arctic FWC is known to have increased since the 1990s and reached a plateau in 2007. We used the 14 years PSY4 simulation to document spatial redistribution of the freshwater and SSH in the Arctic since 2007 resulting from basin-wide changes. Major findings are shown schematically in Figure 13 with annual mean model halocline strength quantified by the APE.

As stated in Regan et al. (2019), the BG extended westward over Mendeleev Ridge in 2011 along the East Siberian Sea slope, inducing an FWC increase along the way (orange arrows in Figure 13a). In 2012, PSY4 showed that large FWC values started to shift toward the center of the Makarov Basin while the BG extended northward (Figure 13b). This coincides with the weakening of the BG under cyclonic winds in 2012 (Zhong et al., 2019). PSY4 showed that freshwater mostly escaped the BG from the west and flowed faster toward the central Makarov Basin. The fresher waters of the gyre are largely composed of Pacific-origin waters (e.g., Hu & Myers, 2013; Proshutinsky et al., 2019) and a northward extension of the BG contributes to a pacification of the Arctic interior as suggested by Polyakov, Alkire, et al. (2020). The concomitant deepening of the isohalines near the North Pole led to the reinforcement of the halocline stratification in the center of the Arctic as quantified by the APE (Figure 13b). From 2017 onwards, the BG retreated from Mendeleev Ridge to the east, likely favored then by the anomalous cyclonic winds in early 2017 (Moore et al., 2018).

After 2012, the model showed that dense AW progressively shoaled along the East Siberian Sea slope (Figure 9) until reaching the Mendeleev Ridge by the end of 2017 (Figure 7g). This is in agreement with a previous model-based study that described the thickening and warming of the AW layer as far as the Mendeleev Ridge in 2010–2017, although no change had been found in the AW layer upper boundary (Grabon et al., 2021). Here, the PSY4 simulations showed that the AW shoaling was accompanied by a weakening of the halocline. This weaker halocline was previously restricted to the continental slope in the Nansen Basin (Polyakov et al., 2018) and reached the East Siberian Sea slope in 2020 (blue arrow in Figure 13b). Such halocline weakening is associated with the ongoing Atlantification (Polyakov et al., 2017). Observations in the Laptev Sea from 2013 to 2018 (Polyakov, Rippeth, et al., 2020) and near Mendeleev Ridge from 2015 to 2017 (Jung et al., 2021) supported such evolution. In parallel, PSY4 showed that the TPD shifted eastward as the Atlantic-origin waters progressed along the Siberian side of the Makarov Basin after 2012, reaching the Mendeleev Ridge (gray arrow in Figure 13). The observed increased contribution of Siberian Sea waters to the TPD is congruent with this eastward shift (Alkire et al., 2019; Bertosio et al., 2020; Shen et al., 2016).

We illustrated changes in the freshwater pathways out of the Amerasian Basin by tracking particles released in the Makarov Basin, near the North Pole, where the FWC increased from 2014 to 2020. During the 2008–2011 period, the upper layer waters from the Makarov Basin exited through Fram Strait. Following the northward extension of the BG in 2011, more waters recirculated within the Canada Basin, contributing to freshwater recharge of the BG from the east, which is in agreement with Hu et al. (2019) and Wilson et al. (2021).

Over the 2014–2016 period, freshwater outflows increased through the western Canadian Archipelago (CA2; +16% compared to 2008–2014) and decreased through Fram Strait (−30%; same period). Recent observation-based studies documented such a reduction both in liquid and solid freshwater outflow at Fram Strait (Karpouzoglou et al., 2022; Sumata et al., 2022). Z. Wang et al. (2017) suggested that the out-of-phase relationship between the freshwater transports through the Canadian Arctic Archipelago and Fram Strait can be explained by anomalous winds at the Arctic Canadian coastline and to the east of Greenland respectively. Zhang et al. (2021) showed that, during the previous historic BG freshwater release period (1983–1995), the BG freshwater exited the Arctic mostly through the Canadian Archipelago rather than Fram Strait. A similar freshwater release may have significant implications for the Labrador Sea hydrographic properties and eventually for the strength of the Atlantic Meridional Overturning Circulation (Proshutinsky et al., 2019). Changes in circulation identified in PSY4 suggested that an analogous scenario might be at play, with a BG freshwater storage two times larger than the previous historical maximum (Proshutinsky et al., 2019).

We further investigated the response of FWC distribution to the changes in atmospheric circulation patterns using the Arctic Oscillation index (from the NOAA NCEP; Figure S5 in Supporting Information S1). Positive peaks in the Arctic Oscillation index (i.e., weak sea level pressure over the Arctic Basin) were followed by an eastward shift of the front, which would be consistent with a cyclonic mode of oceanic circulation characterized by a shifted transpolar front toward the Mendeleev Ridge (Armitage et al., 2018; Morison et al., 2021, 2012; Q. Wang, 2021). Negative Arctic Oscillation index peaks were followed by the return of the front toward the Lomonosov Ridge, consistent with an intensified anticyclonic circulation in the Canada Basin extending toward the Eurasian basin as described by (Morison et al., 2021; Q. Wang, 2021). However, these qualitative covariations should be considered with caution as PSY4 only spanned the relatively short 2007–2020 period.

6. Conclusion

We evaluated the Mercator Ocean simulations over the upper water column in the Arctic Ocean. The model showed capabilities to reproduce observed hydrographic properties and water mass distributions, as well as spatial patterns of FWC and SSH. The model thus provided insights into the interannual evolution of the Arctic upper water column since 2007.

We found that the BG, the major reservoir of Arctic freshwater, extended northward from 2012-onward and consequently increased the FWC in the Makarov Basin, near the North Pole. This freshening of waters in the Makarov Basin resulted in a thickening of the halocline layer and a strengthening of the stratification in the upper water column. In parallel, Atlantic-origin waters shoaled along the East Siberian slope and were associated with a weakened halocline layer.

After 2015, the export of freshwater decreased at Fram Strait (−30% compared to 2008–2014) and increased at the Canadian Archipelago (+16%), followed by an increased export downstream at the Davis Strait a year later. Large freshwater releases could have significant implications for the Labrador Sea hydrographic properties and eventually for the strength of the Atlantic Meridional Overturning Circulation.

Model-derived trajectories in the Amerasian Basin showed the importance of having a sufficient spatial resolution in numerical models to resolve the circulation in the Canadian Archipelago. This study also shows the complementarity of numerical simulations and observations and the great potential of using numerical simulations to broaden the context of Arctic observations. This is especially true with operational systems that, thanks to data assimilation, can minimize biases in the Nordic Seas, the frontier inflow zones of the Arctic Ocean.

Data Availability Statement

Hydrographic data from the UDASH database are available on *PANGEA* (https://doi.pangaea.de/10.1594/PANGAEA.872931; (Behrendt et al., 2018). Temperature and salinity from drifting platform profilers ITPs and mooring data (McLane Moored Profiler) in the Canada Basin are available on the *Beaufort Gyre Exploration Project* website (https://www2.whoi.edu/site/beaufortgyre/data/; Krishfield et al., 2008; Proshutinsky et al., 2009). IAOOS data are available on *SEANOE* (https://doi.org/10.17882/57288). Acoustic Doppler current profiler (ADCP) and temperature and salinity from mooring data in the Bering Strait are available on the *Polar Science Center* website (http://psc.apl.washington.edu/HLD/Bstrait/Data/BeringStraitMooringDataArchive.html; Woodgate et al., 2015). Dynamic ocean topography data are available on the *Center for Polar Observation and Modeling (CPOM)* website (http://www.cpom.ucl.ac.uk/dynamic_topography/; Armitage et al., 2016). PIOMAS model grid data are available on the *Polar Science Center* website (http://psc.apl.uw.edu/research/projects/arctic-sea-ice-volume-anomaly/data/model_grid; Zhang et al., 2003). The Arctic oscillation index is available on the NOAA NCEP website (https://www.cpc.ncep.noaa.gov/products/precip/CWlink/daily_ao_index/ao_index.html). The model outputs are available at Copernicus Marine Environment Monitoring Service (CMEMS; http://marine.copernicus.eu/).

Acknowledgments
Cecilia Bertosio acknowledges support from the IAOOS grant S18JROI002 at Sorbonne University and Marylou Athanase from a postdoc funded by the BMBF research group Seamless Sea Ice Prediction. This work is a contribution to H2020 Arctic Passion project, Grant No. 101003472. This research was a part of the project titled “Korea-Arctic Ocean Warming and Response of Ecosystem (K-AWARE, KOPRI, 1525011760)”, funded by the Ministry of Oceans and Fisheries, Korea. Discussions with H. Regan and P. Prandi are gratefully acknowledged. The authors thank editor Anna Wåhlin and the two anonymous reviewers for their comments which helped improve the manuscript.

References

Aagaard, K., & Woodgate, R. A. (2001). Some thoughts on the freezing and melting of sea ice and their effects on the ocean. *Ocean Modeling*, *3*, 127–135. https://doi.org/10.1016/S1463-5003(01)00005-1

Alkire, M. B., Rember, R., & Polyakov, I. (2019). Discrepancy in the identification of the Atlantic/Pacific front in the central Arctic Ocean: NO vs. nutrient relationships. *Geophysical Research Letters*, *46*(7), 3843–3852. https://doi.org/10.1029/2018GL081837

Armitage, T. W. K., Bacon, S., & Kwok, R. (2018). Arctic sea level and surface circulation response to the Arctic Oscillation. *Geophysical Research Letters*, *45*(13), 6576–6584. https://doi.org/10.1029/2018gl078386

Armitage, T. W. K., Bacon, S., Ridout, A. L., Petty, A. A., Wolbach, S., & Tsamados, M. (2017). Arctic Ocean surface geostrophic circulation 2003–2014. *The Cryosphere*, *11*(4), 1767–1780. https://doi.org/10.5194/tc-11-1767-2017

Armitage, T. W. K., Bacon, S., Ridout, A. L., Thomas, S. F., Aksenov, Y., & Wingham, D. J. (2016). Arctic sea surface height variability and change from satellite radar altimetry and GRACE, 2003–2014. *Journal of Geophysical Research: Oceans*, *121*(6), 4303–4322. https://doi.org/10.1002/2015JC011579

Athanase, M., Provost, C., Artana, C., Pérez-Hernández, M. D., Sennéchael, N., Bertosio, C., et al. (2021). Changes in Atlantic Water circulation patterns and volume transports north of Svalbard over the last 12 years (2008–2020). *Journal of Geophysical Research: Oceans*, *126*, e2020JC016825. https://doi.org/10.1029/2020jc016825

Athanase, M., Provost, C., Pérez Hernández, M. D., Sennéchael, N., Bertosio, C., Artana, C., et al. (2020). Atlantic water modification north of Svalbard in the Mercator physical system from 2007 to 2020. *Journal of Geophysical Research: Oceans*, *125*(10), e2020JC016463. https://doi.org/10.1029/2020JC016463

Athanase, M., Sennéchael, N., Garric, G., Koenig, Z., Boles, E., & Provost, C. (2019). New hydrographic measurements of the upper Arctic western Eurasian Basin in 2017 reveal fresher mixed layer and shallower warm layer than 2005–2012 climatology. *Journal of Geophysical Research: Oceans*, *124*(2), 1091–1114. https://doi.org/10.1029/2018JC014701

Behrendt, A., Sumata, H., Rabe, B., & Schauer, U. (2018). UDASH—Unified database for Arctic and subarctic hydrography. *Earth System Science Data*, *10*(2), 1119–1138. https://doi.org/10.5194/essd-10-1119-2018

Bertosio, C., Provost, C., Sennéchael, N., Artana, C., Athanase, M., Boles, E., et al. (2020). The western Eurasian Basin halocline in 2017: Insights from autonomous NO measurements and the Mercator physical system. *Journal of Geophysical Research: Oceans*, *125*(7), e2020JC016204. https://doi.org/10.1029/2020JC016204

Beszczynska-Möller, A., Woodgate, R. A., Lee, C., Melling, H., & Karcher, M. (2011). A synthesis of exchanges through the main oceanic gateways to the Arctic Ocean. *Oceanography*, *24*(3), 82–99. https://doi.org/10.5670/oceanog.2011.59

Boles, E., Provost, C., Garçon, V., Bertosio, C., Athanase, M., Koenig, Z., & Sennéchael, N. (2020). Under-ice phytoplankton blooms in the central Arctic Ocean: Insights from the first biogeochemical IAOOS platform drift in 2017. *Journal of Geophysical Research: Oceans*, *125*(3), e2019JC015608. https://doi.org/10.1029/2019JC015608

Carmack, E. C. (2007). The alpha/beta ocean distinction: A perspective on freshwater fluxes, convection, nutrients and productivity in high-latitude seas. *Deep-Sea Research Part II: Topical Studies in Oceanography*, *54*(23), 2578–2598. https://doi.org/10.1016/j.dsr2.2007.08.018

Carmack, E. C., Yamamoto-Kawai, M., Haine, T. W. N., Bacon, S., Bluhm, B. A., Lique, C., et al. (2016). Freshwater and its role in the Arctic Marine System: Sources, disposition, storage, export, and physical and biogeochemical consequences in the Arctic and global oceans. *Journal of Geophysical Research: Biogeosciences*, *121*(3), 675–717. https://doi.org/10.1002/2015JG003140

Corlett, W. B., & Pickart, R. S. (2017). The Chukchi slope current. *Progress in Oceanography*, *153*, 50–65. https://doi.org/10.1016/j.pocean.2017.04.005

Curry, B., Lee, C. M., & Petrie, B. (2011). Volume, freshwater, and heat fluxes through Davis Strait, 2004–2005. *Journal of Physical Oceanography*, *41*(3), 429–436. https://doi.org/10.1175/2010JPO4536.1

Doddridge, E. W., Meneghello, G., Marshall, J., Scott, J., & Lique, C. (2019). A three-way balance in the Beaufort Gyre: The ice-ocean governor, wind stress, and eddy diffusivity. *Journal of Geophysical Research: Oceans*, *124*(5), 3107–3124. https://doi.org/10.1029/2018JC014897

Fichefet, T., & Maqueda, M. A. (1997). Sensitivity of a global sea ice model to the treatment of ice thermodynamics and dynamics. *Journal of Geophysical Research*, *102*, 12609–12646. https://doi.org/10.1029/97JC00480

Fillipi, J.-B., Komatsu, T., & Tanaka, K. (2010). Simulation of drifting seaweeds in East China Sea. *Ecological Informatics*, *5*(1), 67–72. https://doi.org/10.1016/j.ecoinf.2009.08.011

Good, S. A., Martin, M. J., & Rayner, N. A. (2013). EN4: Quality controlled ocean temperature and salinity profiles and monthly objective analyses with uncertainty estimates. *Journal of Geophysical Research: Oceans*, *118*, 6704–6716. https://doi.org/10.1002/2013JC009067

Grabon, J. S., Toole, J. M., Nguyen, A. T., & Krishfield, R. A. (2021). An analysis of Atlantic Water in the Arctic Ocean using the Arctic subpolar gyre state estimate and observations. *Progress in Oceanography*, *198*, 102685. https://doi.org/10.1016/j.pocean.2021.102685

Haine, T. W. N., Curry, B., Gerdes, R., Hansen, E., Karcher, M., Lee, C., et al. (2015). Arctic freshwater export: Status, mechanisms, and prospects. *Global and Planetary Change*, *125*, 13–35. https://doi.org/10.1016/j.gloplacha.2014.11.013

Hu, X., & Myers, P. G. (2013). A Lagrangian view of Pacific water inflow pathways in the Arctic Ocean during model spin-up. *Ocean Modeling*, *71*, 66–80. https://doi.org/10.1016/j.ocemod.2013.06.007

Hu, X., Myers, P. G., & Lu, Y. (2019). Pacific water pathway in the Arctic Ocean and Beaufort Gyre in two simulations with different horizontal resolutions. *Journal of Geophysical Research: Oceans*, *124*(8), 6414–6432. https://doi.org/10.1029/2019JC015111

Jahn, A., Aksenov, Y., de Cuevas, B. A., de Steur, L., Häkkinen, S., Hansen, E., et al. (2012). Arctic Ocean freshwater: How robust are model simulations? *Journal of Geophysical Research: Oceans*, *117*(C8). https://doi.org/10.1029/2012JC007907

Jung, J., Cho, K.-H., Park, T., Yoshizawa, E., Lee, Y., Yang, E. J., et al. (2021). Atlantic-origin cold saline water intrusion and shoaling of the nutricline in the Pacific Arctic. *Geophysical Research Letters*, *48*(6), e2020GL090907. https://doi.org/10.1029/2020GL090907

Karcher, M., Smith, J. N., Kauker, F., Gerdes, R., & Smethie, W. M. (2012). Recent changes in Arctic Ocean circulation revealed by iodine-129 observations and modeling. *Journal of Geophysical Research: Oceans*, *117*(C8). https://doi.org/10.1029/2011JC007513

Karpouzoglou, T., de Steur, L., Smedsrud, L. H., & Sumata, H. (2022). Observed changes in the Arctic freshwater outflow in Fram Strait. *Journal of Geophysical Research: Oceans*, *127*, e2021JC018122. https://doi.org/10.1029/2021JC018122

Koenig, Z., Provost, C., Sennéchael, N., Garric, G., & Gascard, J.-C. (2017). The Yermak Pass branch: A major pathway for the Atlantic Water north of Svalbard? *Journal of Geophysical Research: Oceans*, *122*(12), 9332–9349. https://doi.org/10.1002/2017JC013271

Koenig, Z., Provost, C., Villacieros-Robineau, N., Sennéchael, N., Meyer, A., Lellouche, J.-M., & Garric, G. (2017). Atlantic Waters inflow north of Svalbard: Insights from IAOOS observations and Mercator Ocean global operational system during N-ICE2015. *Journal of Geophysical Research: Oceans*, *122*(2), 1254–1273. https://doi.org/10.1002/2016JC012424

Krishfield, R., Toole, J., Proshutinsky, A., & Timmermans, M.-L. (2008). Automated ice-tethered profilers for seawater observations under pack ice in all seasons. *Journal of Atmospheric and Oceanic Technology*, *25*(11), 2091–2105. https://doi.org/10.1175/2008JTECHO587.1

Kwok, R., Spreen, G., & Pang, S. (2013). Arctic sea ice circulation and drift speed: Decadal trends and ocean currents. *Journal of Geophysical Research: Oceans*, *118*(5), 2408–2425. https://doi.org/10.1002/jgrc.20191

Lellouche, J. M., Greiner, E., Galloudec, O. L., Garric, G., Regnier, C., Drevillon, M., et al. (2018). Recent updates to the Copernicus Marine Service global ocean monitoring and forecasting real-time 1/12° high-resolution system. *Ocean Science*, *14*(5), 1093–1126. https://doi.org/10.5194/os-14-1093-2018

Lind, S., Ingvaldsen, R. B., & Furevik, T. (2018). Arctic warming hotspot in the northern Barents Sea linked to declining sea-ice import. *Nature Climate Change*, *8*(7), 634–639. https://doi.org/10.1038/s41558-018-0205-y

Lique, C., Holland, M. M., Dibike, Y. B., Lawrence, D. M., & Screen, J. A. (2016). Modeling the Arctic freshwater system and its integration in the global system: Lessons learned and future challenges. *Journal of Geophysical Research: Biogeosciences*, *121*(3), 540–566. https://doi.org/10.1002/2015JG003120

Madec, G., & Imbard, M. (1996). A global ocean mesh to overcome the North Pole singularity. *Climate Dynamics*, *12*, 381–388. https://doi.org/10.1007/bf00211684

Madec, G., & the NEMO team: NEMO ocean engine. (2008). *Note du Pôle de modélisation, Institut Pierre-Simon Laplace (IPSL)*, France, No. 27 ISSN, 1288–1619.

McClelland, J. W., Holmes, R. M., Dunton, K. H., & Macdonald, R. W. (2012). The Arctic Ocean estuary. *Estuaries and Coasts*, *35*(2), 353–368. https://doi.org/10.1007/s12237-010-9357-3

McDougall, T. J., & Barker, P. M. (2011). *Getting started with TEOS-10 and the Gibbs Seawater (GSW) Oceanographic Toolbox*. 28pp. SCOR/IAPSO WG127 (ISBN: 978-0-646-55621-5).

Moore, G. W. K., Schweiger, A., Zhang, J., & Steele, M. (2018). Collapse of the 2017 winter Beaufort high: A response to Thinning sea ice? *Geophysical Research Letters*, *45*(6), 2860–2869. https://doi.org/10.1002/2017GL076446

Morison, J., Kwok, R., Dickinson, S., Andersen, R., Peralta-Ferriz, C., Morison, D., et al. (2021). The cyclonic mode of Arctic Ocean circulation. *Journal of Physical Oceanography*, *51*(4), 1053–1075. https://doi.org/10.1175/JPO-D-20-0190.1

Morison, J., Kwok, R., Peralta-Ferriz, C., Alkire, M., Rigor, I., Andersen, R., & Steele, M. (2012). Changing Arctic Ocean freshwater pathways. *Nature*, *481*(7379), 66–70. https://doi.org/10.1038/nature10705

Morison, J., Steele, M., & Andersen, R. (1998). Hydrography of the upper Arctic Ocean measured from the nuclear submarine U.S.S. Pargo. *Deep-Sea Research Part I: Oceanographic Research Papers*, *45*(1), 15–38. https://doi.org/10.1016/S0967-0637(97)00025-3

Pisareva, M. N., Pickart, R. S., Spall, M. A., Nobre, C., Torres, D. J., Moore, G. W. K., & Whitledge, T. E. (2015). Flow of Pacific water in the western Chukchi Sea: Results from the 2009 RUSALCA expedition. *Deep-Sea Research Part I: Oceanographic Research Papers*, *105*, 53–73. https://doi.org/10.1016/j.dsr.2015.08.011

Polyakov, I. V., Alkire, M. B., Bluhm, B. A., Brown, K. A., Carmack, E. C., Chierici, M., et al. (2020). Borealization of the Arctic Ocean in response to anomalous advection from sub-Arctic seas. *Frontiers in Marine Science*, *7*. https://doi.org/10.3389/fmars.2020.00491

Polyakov, I. V., Pnyushkov, A. V., Alkire, M. B., Ashik, I. M., Baumann, T. M., Carmack, E. C., et al. (2017). Greater role for Atlantic inflows on sea-ice loss in the Eurasian Basin of the Arctic Ocean. *Science*, *356*(6335), 285–291. https://doi.org/10.1126/science.aai8204

Polyakov, I. V., Pnyushkov, A. V., & Carmack, E. C. (2018). Stability of the Arctic halocline: A new indicator of Arctic climate change. *Environmental Research Letters*, *13*(12), 125–008. https://doi.org/10.1088/1748-9326/aaec1e

Polyakov, I. V., Rippeth, T. P., Fer, I., Alkire, M. B., Baumann, T. M., Carmack, E. C., et al. (2020). Weakening of cold halocline layer exposes sea ice to oceanic heat in the eastern Arctic Ocean. *Journal of Climate*, *33*(18), 8107–8123. https://doi.org/10.1175/JCLI-D-19-0976.1

Proshutinsky, A., Bourke, R. H., & McLaughlin, F. A. (2002). The role of the Beaufort Gyre in Arctic climate variability: Seasonal to decadal climate scales. *Geophysical Research Letters*, *29*(23), 15-1–15-4. https://doi.org/10.1029/2002GL015847

Proshutinsky, A., Dukhovskoy, D., Timmermans, M.-L., Krishfield, R., & Bamber Jonathan, L. (2015). Arctic circulation regimes. *Philosophical Transactions of the Royal Society A: Mathematical, Physical & Engineering Sciences*, *373*(2052), 20140160. https://doi.org/10.1098/rsta.2014.0160

Proshutinsky, A., & Johnson, M. A. (1997). Two circulation regimes of the wind-driven Arctic Ocean. *Journal of Geophysical Research: Oceans*, *102*(C6), 12493–12514. https://doi.org/10.1029/97JC00738

Proshutinsky, A., Krishfield, R., Timmermans, M.-L., Toole, J., Carmack, E., McLaughlin, F., et al. (2009). Beaufort Gyre freshwater reservoir: State and variability from observations. *Journal of Geophysical Research*, *114*(C1). https://doi.org/10.1029/2008JC005104

Proshutinsky, A., Krishfield, R., Toole, J. M., Timmermans, M.-L., Williams, W., Zimmermann, S., et al. (2019). Analysis of the Beaufort Gyre freshwater content in 2003–2018. *Journal of Geophysical Research: Oceans*, *124*(12), 9658–9689. https://doi.org/10.1029/2019JC015281

Rabe, B., Karcher, M., Kauker, F., Schauer, U., Toole, J. M., Krishfield, R. A., et al. (2014). Arctic Ocean basin liquid freshwater storage trend 1992–2012. *Geophysical Research Letters*, *41*(3), 961–968. https://doi.org/10.1002/2013GL058121

Rahmstorf, S., Box, J. E., Feulner, G., Mann, M. E., Robinson, A., Rutherford, S., & Schaffernicht, E. J. (2015). Exceptional twentieth-century slowdown in Atlantic Ocean overturning circulation. *Nature Climate Change*, *5*(5), 475–480. https://doi.org/10.1038/nclimate2554

Regan, H., Lique, C., & Armitage, T. W. K. (2019). The Beaufort Gyre extent, shape, and location between 2003 and 2014 from satellite observations. *Journal of Geophysical Research: Oceans*, *124*(2), 844–862. https://doi.org/10.1029/2018JC014379

Regan, H., Lique, C., Talandier, C., & Meneghello, G. (2020). Response of total and eddy kinetic energy to the recent spin up of the Beaufort Gyre. *Journal of Physical Oceanography*, *50*(3), 575–594. https://doi.org/10.1175/JPO-D-19-0234.1

Rudels, B., Anderson, L. G., & Jones, E. P. (1996). Formation and evolution of the surface mixed layer and halocline of the Arctic Ocean. *Journal of Geophysical Research: Oceans*, *101*(C4), 8807–8821. https://doi.org/10.1029/96JC00143

Rudels, B., Korhonen, M., Schauer, U., Pisarev, S., Rabe, B., & Wisotzki, A. (2015). Circulation and transformation of Atlantic Water in the Eurasian Basin and the contribution of the Fram Strait inflow branch to the Arctic Ocean heat budget. *Progress in Oceanography*, *132*, 128–152. https://doi.org/10.1016/j.pocean.2014.04.003

Schweiger, A., Lindsay, R., Zhang, J., Steele, M., Stern, H., & Kwok, R. (2011). Uncertainty in modeled Arctic sea ice volume. *Journal of Geophysical Research: Oceans*, *116*(C8). https://doi.org/10.1029/2011JC007084

Serreze, M. C., Barrett, A. P., Slater, A. G., Woodgate, R. A., Aagaard, K., Lammers, R. B., et al. (2006). The large-scale freshwater cycle of the Arctic. *Journal of Geophysical Research: Oceans*, *111*, C11010. https://doi.org/10.1029/2005JC003424

Shen, Y., Benner, R., Robbins, L., & Wynn, J. (2016). Sources, distributions, and dynamics of dissolved organic matter in the Canada and Makarov Basins. *Frontiers in Marine Science*, *3*. https://doi.org/10.3389/fmars.2016.00198

Shimada, K., Itoh, M., Nishino, S., McLaughlin, F., Carmack, E. C., & Proshutinsky, A. (2005). Halocline structure in the Canada Basin of the Arctic Ocean. *Geophysical Research Letters*, *32*(3). https://doi.org/10.1029/2004GL021358

Solomon, A., Heuzé, C., Rabe, B., Bacon, S., Bertino, L., Heimbach, P., et al. (2020). Freshwater in the Arctic Ocean 2010–2019. *Ocean Science Discussions*, 1–28. https://doi.org/10.5194/os-2020-113

Spall, M. A., Pickart, R. S., Fratantoni, P. S., & Plueddemann, A. J. (2008). Western Arctic Shelfbreak eddies: Formation and transport. *Journal of Physical Oceanography*, *38*(8), 1644–1668. https://doi.org/10.1175/2007JPO3829.1

Stabeno, P., Kachel, N., Ladd, C., & Woodgate, R. (2018). Flow patterns in the eastern Chukchi Sea: 2010–2015. *Journal of Geophysical Research: Oceans*, *123*(2), 1177–1195. https://doi.org/10.1002/2017JC013135

Sumata, H., de Steur, L., Gerland, S., Divine, D. V., & Pavlova, O. (2022). Unprecedented decline of Arctic sea ice outflow in 2018. *Nature Communications*, *13*, 1747. https://doi.org/10.1038/s41467-022-29470-7

Swift, J. H., Jones, E. P., Aagaard, K., Carmack, E. C., Hingston, M., MacDonald, R. W., et al. (1997). Waters of the Makarov and Canada basins. *Deep-Sea Research Part II: Topical Studies in Oceanography*, *44*(8), 1503–1529. https://doi.org/10.1016/S0967-0645(97)00055-6

Thompson, D. W. J., & Wallace, J. M. (1998). The Arctic oscillation signature in the wintertime geopotential height and temperature fields. *Geophysical Research Letters*, *25*(9), 1297–1300. https://doi.org/10.1029/98GL00950

Timmermans, M.-L., & Jayne, S. R. (2016). The Arctic Ocean spices up. *Journal of Physical Oceanography*, *46*(4), 1277–1284. https://doi.org/10.1175/JPO-D-16-0027.1

Timmermans, M.-L., & Marshall, J. (2020). Understanding Arctic Ocean circulation: A review of ocean dynamics in a changing climate. *Journal of Geophysical Research: Oceans*, *125*, e2018JC014378. https://doi.org/10.1029/2018jc014378

Toole, J. M., Krishfield, R. A., Timmermans, M.-L., & Proshutinsky, A. (2011). The ice-tethered profiler: Argo of the Arctic. *Oceanography*, *24*(3), 126–135. https://doi.org/10.5670/oceanog.2011.64

Wang, Q. (2021). Stronger variability in the Arctic Ocean induced by sea ice decline in a warming climate: Freshwater storage, dynamic sea level and surface circulation. *Journal of Geophysical Research: Oceans*, *126*(3), e2020JC016886. https://doi.org/10.1029/2020JC016886

Wang, Q., Ilicak, M., Gerdes, R., Drange, H., Aksenov, Y., Bailey, D. A., et al. (2016). An assessment of the Arctic Ocean in a suite of interannual CORE-II simulations. Part I: Sea ice and solid freshwater. *Ocean Modeling*, *99*, 110–132. https://doi.org/10.1016/j.ocemod.2015.12.008

Wang, X., Key, J., Kwok, R., & Zhang, J. (2016). Comparison of Arctic sea ice thickness from satellites, aircraft, and PIOMAS data. *Remote Sensing*, *8*(9), 713. https://doi.org/10.3390/rs8090713

Wang, Z., Hamilton, J., & Su, J. (2017). Variations in freshwater pathways from the Arctic Ocean into the North Atlantic Ocean. *Progress in Oceanography*, *155*, 54–73. https://doi.org/10.1016/j.pocean.2017.05.012

Wilson, C., Aksenov, Y., Rynders, S., Kelly, S. J., Krumpen, T., & Coward, A. C. (2021). Significant variability of structure and predictability of Arctic Ocean surface pathways affects basin-wide connectivity. *Communications Earth & Environment*, *2*(1), 1–10. https://doi.org/10.1038/s43247-021-00237-0

Woodgate, R. A. (2018). Increases in the Pacific inflow to the Arctic from 1990 to 2015, and insights into seasonal trends and driving mechanisms from year-round Bering Strait mooring data. *Progress in Oceanography*, *160*, 124–154. https://doi.org/10.1016/j.pocean.2017.12.007

Woodgate, R. A., & Peralta-Ferriz, C. (2021). Warming and freshening of the Pacific inflow to the Arctic from 1990–2019 implying dramatic shoaling in Pacific Winter Water ventilation of the Arctic water column. *Geophysical Research Letters*, *48*, e2021GL092528. https://doi.org/10.1029/2021GL092528

Woodgate, R. A., Stafford, K., & Prahl, F. (2015). A synthesis of year-round interdisciplinary mooring measurements in the Bering Strait (1990–2014) and the RUSALCA years (2004–2011). *Oceanography*, *28*, 46–67. https://doi.org/10.5670/oceanog.2015.57

Woodgate, R. A., Weingartner, T. J., & Lindsay, R. (2012). Observed increases in Bering Strait oceanic fluxes from the Pacific to the Arctic from 2001 to 2011 and their impacts on the Arctic Ocean water column. *Geophysical Research Letters*, *39*(24). https://doi.org/10.1029/2012GL054092

Zhang, J., & Rothrock, D. A. (2003). Modeling global sea ice with a thickness and enthalpy distribution model in generalized curvilinear coordinates. *Monthly Weather Review*, *131*(5), 681–697. https://doi.org/10.1175/1520-0493(2003)131<0845:MGSIWA>2.0.CO;2

Zhang, J., Steele, M., Runciman, K., Dewey, S., Morison, J., Lee, C., et al. (2016). The Beaufort Gyre intensification and stabilization: A model-observation synthesis. *Journal of Geophysical Research: Oceans*, *121*(11), 7933–7952. https://doi.org/10.1002/2016JC012196

Zhang, J., Weijer, W., Steele, M., Cheng, W., Verma, T., & Veneziani, M. (2021). Labrador Sea freshening linked to Beaufort Gyre freshwater release. *Nature Communications*, *12*(1), 1229. https://doi.org/10.1038/s41467-021-21470-3

Zhong, W., Zhang, J., Steele, M., Zhao, J., & Wang, T. (2019). Episodic extrema of surface stress energy input to the western Arctic Ocean contributed to step changes of freshwater content in the Beaufort Gyre. *Geophysical Research Letters*, *46*(21), 12173–12182. https://doi.org/10.1029/2019GL084652